Colloids and Surfaces B: Biointerfaces 266 (2026) 115784

Contents lists available at ScienceDirect

Colloids and Surfaces B: Biointerfaces

journal homepage: www.elsevier.com/locate/colsurfb

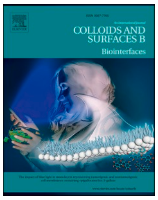

Anisotropic magnetic particles with different dimensions, morphologies and surface grafting for magnetic field-assisted biofilm removal

Nika Zaveršek [a,b], Maja Caf [c,d], Vincent Pautu [e], Laurine Marger [f], Parvaneh Esmaeilnejad-Ahranjani [c,1], Nika Janež [a], Tanja Zupan [a], Fabrice Marger [f], Ana Parga [f,g], Saša Haberl-Meglič [h], Mustapha Mekki [f], Aleš Berlec [a,d], Irena Milošević [e], Slavko Kralj [c,d,*], Jerica Sabotič [a,**]

[a] *Jožef Stefan Institute, Department of Biotechnology, Jamova ulica 39, Ljubljana 1000, Slovenia*
[b] *University of Ljubljana, Biotechnical faculty, Jamnikarjeva 101, Ljubljana 1000, Slovenia*
[c] *Jožef Stefan Institute, Department for Materials Synthesis, Jamova ulica 39, Ljubljana 1000, Slovenia*
[d] *University of Ljubljana, Faculty of Pharmacy, Aškerčeva ulica 7, Ljubljana 1000, Slovenia*
[e] *HES-SO - University of Applied Sciencesand Arts Western Switzerland, School of Engineering, Architecture and Landscape of Geneva (HEPIA), Rue de la Prairie 4, Geneva CH1202, Switzerland*
[f] *University of Geneva, University Clinics of Dental Medicine, Biomaterials Laboratory, Division of Fixed Prosthodontics and Biomaterials, Michel-Servet 1, Geneva 1204, Switzerland*
[g] *University of Geneva, Department of Microbiology and Molecular Medicine, 24 rue du Général-Dufour, Geneva 1211, Switzerland*
[h] *University of Ljubljana, Faculty of Electrical Engineering, Tržaška cesta 25, Ljubljana 1000, Slovenia*

ARTICLE INFO

Keywords:
Magnetic microrobots
Magnetic assembly
Anisotropic magnetic particles
Silver nanoparticles
Biofilm
Magneto-mechanical actuation
Listeria innocua

ABSTRACT

Microorganisms in biofilms are protected from environmental stressors and therefore exhibit strong resistance to conventional removal strategies, including chemical disinfectants and antibiotics. In this study, we systematically evaluated nanomaterial-based removal methods on *Listeria innocua* biofilms. Anisotropic magnetic particles, composed of iron oxide, and silver nanoparticles, known for their intrinsic antibacterial properties, were used to assess the potential of nanostructure-triggered biofilm disruption. We investigated how particle surface roughness and size affect biofilm removal under magnetic actuation, using both classical colony-forming unit quantification (viability assessment) and fluorescence-based detection via a reporter protein. The surface roughness and size of anisotropic magnetic particles only modestly affected biofilm disruption. Conversely, a synergistic effect was observed when anisotropic magnetic particles were grafted with silver nanoparticles. Furthermore, we used *Enterococcus faecalis* and *Candida albicans* biofilms and observed pronounced species-dependent variability of the silver-based treatments. Our results indicate that hybrid magneto–chemical strategies represent a promising and likely necessary approach for reliable and robust biofilm removal.

1. Introduction

Biofilms present a significant challenge, as they form on a wide range of biotic and abiotic surfaces and enable microorganisms to persist as ongoing sources of contamination and potential illness. Biofilm-related infections frequently arise from biofilm formation on teeth, tissues, implants, and medical equipment in hospital settings. Biofilms are also a common cause of food recalls due to colonization of surfaces and contamination of water supplies in food industry environments [1–3]. Biofilms consist of microbial cells and a matrix of extracellular polymeric substances (EPS) that is crucial for the functional and structural integrity of biofilms. The EPS matrix is composed of extracellular proteins, extracellular DNA, and exopolysaccharides, the presence and composition of which depend on the bacterial species [1,4].

---

* Corresponding author at: Jožef Stefan Institute, Department for Materials Synthesis, Jamova ulica 39, Ljubljana 1000, Slovenia.
** Corresponding author.
E-mail addresses: slavko.kralj@ijs.si (S. Kralj), jerica.sabotic@ijs.si (J. Sabotič).
[1] Current address: Department of Research and Development, Razi Vaccine and Serum Research Institute, Agricultural Research, Education and Extension Organization (AREEO), P.O. Box: 31975/148, Karaj, Iran.

https://doi.org/10.1016/j.colsurfb.2026.115784
Received 20 March 2026; Received in revised form 24 April 2026; Accepted 4 May 2026

Microorganisms within biofilms are protected from stress, dehydration, and antibacterial agents, making them more resistant to cleaning fluids, disinfectants, and antibiotics [5,6].

Listeria innocua are harmless Gram-positive bacteria frequently isolated from food industry environments and food products [7]. They are proficient at forming biofilms and can be found alongside the closely related species *Listeria monocytogenes*. However, *L. monocytogenes* is highly pathogenic to humans and animals, causing infections that lead to high hospitalization and mortality rates among high-risk individuals. *Listeria* species adhere very firmly to various biotic and abiotic surfaces and form biofilms, making them a good model for persistent biofilms [8]. Both above-mentioned species coexist in the same environments, and thus *L. innocua* can mask the presence of *L. monocytogenes* or enhance its growth through cooperation in biofilms [9]. Therefore, controlling *L. innocua* biofilms serves as a useful strategy for restricting *L. monocytogenes* growth in the food industry [9–11]. Beyond food-related contexts, biofilms formed by the Gram-positive bacterium *Enterococcus faecalis* and the yeast *Candida albicans* are clinically relevant in dentistry and implantology, where biofilm growth is often responsible for unsuccessful treatments with conventional disinfectants and antimicrobial agents [12,13].

Classical biofilm removal strategies include physical methods (e.g., non-thermal plasma [14] and high hydrostatic pressure [15]), chemical methods (e.g., chlorine-based agents and oxidants [16,17]), and biological methods (e.g., enzymes [18], biosurfactants [19], and bacteriophages [20]). Physical methods are difficult to implement at the industrial scale and are frequently insufficient when used alone [2,10]. Chemical methods, although widely used, remain species- and condition-dependent and are increasingly limited by the emergence of resistance, particularly in relation to chlorine-based agents [2,14]. Enzymes are also useful as they degrade EPS components; however, they tend to be more species-specific and must often be combined with mechanical treatments or sanitizers to achieve sufficient effectiveness. Moreover, biofilms are highly complex, varying in their characteristics and species, which increases the likelihood of resistance to removal methods. To address this challenge, the development of new methods for biofilm removal is essential [6,10].

In recent years, nanomaterials have attracted considerable attention due to their high reactivity, robust chemical and thermal stability, large surface-to-volume ratio, and cost-effective production [21,22]. Furthermore, their tunable physicochemical properties additionally expand their utility in biomedical applications, particularly in combating biofilms. Because of their nanoscale dimensions, engineered nanoparticles (NPs) can penetrate dense biological barriers, traverse biofilm matrices, and release antimicrobial agents at otherwise inaccessible sites. Further functionalization of NP surfaces enhances targeted delivery. Additionally, certain inorganic NPs, such as silver, exhibit intrinsic antimicrobial activity, enabling their direct use as biofilm-disrupting agents [21–23].

Various nanomaterials exist, of which stable assemblies of multiple magnetic iron oxide NPs (IONPs) are particularly promising due to their superparamagnetism, ease of surface modification, and responsiveness to external magnetic fields, enabling both precise magnetic guidance and magneto-mechanical actuation [24,25]. In addition to their established applications in magnetic resonance imaging, magnetic particle imaging, magnetic hyperthermia, and drug delivery [22,26,27], assemblies of multiple IONPs offer unique advantages for biofilm eradication [28]. They can disrupt microbial communities (through reactive oxygen species generation), enhance antimicrobial delivery, mechanically disturb the EPS matrix, and enable localized magnetic hyperthermia [29,30]. Functionalized IONP assemblies carrying antimicrobial agents can be precisely directed to infection sites using external magnetic field gradients, enabling localized drug release and minimizing systemic side effects [22]. Moreover, their ability to generate heat under an alternating magnetic field makes them highly promising for magnetic hyperthermia [31]. Importantly, when physically propelled or oscillated by exposure to external magnetic field actuators, IONPs in the form of particles with anisotropic shapes can mechanically penetrate the EPS matrix, creating microscale channels that compromise biofilm integrity and significantly improve antimicrobial penetration [25,32,33]. Collectively, these multifaceted properties position IONP assemblies as a powerful platform for next-generation biofilm therapies, offering innovative strategies to overcome the persistent limitations of conventional antibiotics.

Silver nanoparticles (AgNPs) are known for their antibacterial effects against various organisms [34], and their antibiofilm effects have also been reported [35]. However, these effects are not entirely general and are strongly influenced by AgNP design [36,37].

In this work, we investigated the potential of magneto–mechanical disruption as a strategy for removing resilient biofilms, using persistent *L. innocua* biofilms as a model system. We systematically studied various properties of anisotropic magnetic particles (AMPs) and assessed the biofilm removal potential of a hybrid magneto–chemical approach based on engineered AMPs and AgNPs.

2. Materials and methods

2.1. Materials

Iron(III) sulfate hydrate, iron(II) sulfate heptahydrate, ammonium hydroxide (25%), acetone (99.5%), and citric acid monohydrate (99%) were purchased from VWR Chemicals. Dichloromethane (99.5%) was obtained from J.T. Baker. Tetraethyl orthosilicate (TEOS), N,N-diisopropylethylamine (DIPEA, ≥ 99%), absolute ethanol (99.5%), polyvinylpyrrolidone (PVP, Mw = 40 kDa), and triethanolamine (TEA, ≥ 99%) were sourced from Sigma-Aldrich. Cetyltrimethylammonium bromide (CTAB, 98%) and NaCl (≥ 99.5%) were supplied by Thermo Fisher Scientific, hydrobromic acid (48%) by Fluka, and tris(hydroxymethyl)aminomethane (TRIS, 99.8%) by Acros Organics. Cyclohexane (99.8%) was purchased from Carlo Erba Reagents, and hexadecyltrimethylammonium p-toluenesulfonate (99.0%) and N,N-dimethylformamide (DMF, 99.9%) were acquired from Merck. Ammonium nitrate (> 99%) was purchased from Chemlab, and both (3-aminopropyl)triethoxysilane (APTES, 98%) and succinic anhydride (SA, 99%) were purchased from Alfa Aesar. Ricinoleic acid (> 80%) was acquired from TCI Chemicals. Silver nitrate ($AgNO_3$, ≥ 99%), tannic acid (≥ 95%), nitric acid (≥ 65%), sodium hydroxide (NaOH, ≥ 98%) were purchased from Carl Roth. Thiol-polyethylene glycol-acid, N-hydroxysulfosuccinimide sodium salt (sulfo NHS), N-(3-dimethylaminopropyl)-N′-ethylcarbodiimide-hydrochloride (EDC), and phosphate-buffered saline (PBS, pH 7.4, tablets) were purchased from Brunschwig. Water was purified using an Adrona E30 purification system (Adrona Ltd., Riga, Latvia). Silica NPs (SiO_2NPs) with a size of 50 nm were comprehensively described and thoroughly characterized in Polajžer et al. [38].

2.2. Syntheses of different AMPs

2.2.1. Synthesis of nanochains (NCs) with different silica shell morphologies

Magnetic NCs were synthesized in a multistep process. First, nanoclusters with a mean diameter of approximately 100 nm were prepared as previously reported [39–41]. These clusters were then magnetically assembled into linear chain-like structures of approximately 900 nm in length through magnetic alignment, as described in detail elsewhere [42]. The dynamically formed NCs were subsequently coated with three distinct types of silica shells, as detailed in our earlier studies [33,41].

For smooth silica-coated NCs (NC-sSi), NCs (100 mg) were resuspended in distilled water to a final volume of 114 mL and sonicated for 1 min. The suspension was then mixed with 18 mL of aqueous ammonia (25 wt%) and sonicated again for 1 min. Subsequently, 300 mL of TEOS solution (0.02 M in ethanol) was added, and the mixture was stirred overnight. The next day, the particles were washed twice with ethanol, twice with distilled water, and finally resuspended in water at a concentration of 10 mg/mL.

For highly rough silica-coated NCs (NC-hrSi), 75 mL of CTAB (0.26 M) solution was prepared, of which 5 mL was used to dissolve 137 mg of tris(hydroxymethyl)aminomethane. NCs (100 mg) were dispersed in the remaining CTAB solution, and then the tris(hydroxymethyl)aminomethane–CTAB mixture was added gradually. The resulting suspension was sonicated for 1 min, transferred to a round-bottom flask, placed in an oil bath at 50 °C, and stirred at 600 rpm for 10 min. A solution of TEOS (0.938 mL) in cyclohexane (11 mL) was then added to the NC suspension. The reaction proceeded under continuous stirring for 1.5 h, after which a second identical amount of TEOS in cyclohexane was introduced. The mixture was then stirred overnight at 50 °C. To remove residual surfactant, ammonium nitrate (2 g) was dissolved in ethanol (100 mL) at 60 °C, and then NCs (100 mg) were added and stirred for 1 h. Particles were washed twice with ethanol and were then resuspended in ethanol (50 mL). If the isoelectric point exceeded pH 4.0, the process was repeated. After the final wash, particles were resuspended in water to a final concentration of 10 mg/mL.

For moderately rough silica-coated NCs (NC-mrSi), 52 mL of hexadecyltrimethylammonium p-toluenesulfonate (0.025 M) was heated to 50 °C and then mixed with NCs (100 mg) and TEOS (2.5 mL). After 10 min, triethanolamine (6.25 μL) was added, and the mixture was stirred overnight at 50 °C. Residual templating surfactants were removed using the ammonium nitrate washing procedure described for NC-hrSi. The particles were then resuspended in water to a final concentration of 10 mg/mL.

2.2.2. Synthesis of magnetic microrods

Magnetic microrods were synthesized by magnetic assembly of IONPs followed by silica deposition [43]. IONPs were synthesized by co-precipitation of Fe^{2+} (27 mM) and Fe^{3+} (14 mM) salts in aqueous solution following established protocols [44]. Co-precipitation was induced by stepwise addition of 25% aqueous ammonia: first adjusting the pH to 3 for 30 min and then to 11.6 for another 30 min. The synthesized nanocrystals were collected with an NdFeB magnet, washed three times with ammonia solution (pH 10.5), and redispersed in water (120 mL). For colloidal stabilization with citric acid [45], 5 mL of citric acid solution (0.5 g/mL) was added to the dispersion. The pH was adjusted to 5.2, and the mixture was stirred at 80 °C for 90 min. Subsequently, the pH was raised to 10.2 with 25% aqueous ammonia, and the suspension was centrifuged at 5000 g for 5 min to remove aggregates. The resulting magnetic NP suspension was used for further magnetic assembly [46].

To 75 mL of this suspension, 1.5 mL of 25% aqueous ammonia was added under stirring at 400 rpm for 2 min to initiate TEOS hydrolysis and condensation. TEOS solution (0.172 M) in ethanol was then added dropwise, and after 1 min, saturated NaCl solution (3 mL) was added to promote magnetic assembly and rod-like formation. The mixture was stirred for 2 min, exposed to a 24 mT magnetic field, and left overnight to enable the formation of micron-sized rods by silica deposition and structure strengthening. The magnetic microrods were purified by magnetic separation and repeated washing. To enhance microrod stability, an additional thin silica shell was deposited. The magnetic microrods were dispersed in a mixture of water (100 mL) and ethanol (250 mL), and then 1.65 mL of 25% aqueous ammonia was added, followed by the gradual addition of 17 mL of TEOS (0.79 M) in ethanol under stirring at 250 rpm. Two additional 1.65 mL aliquots of ammonia were added at 1 h intervals to maintain TEOS hydrolysis and condensation. The reaction proceeded for an additional 2 h. Silica-coated microrods were purified by magnetic separation and washing with deionized water. After the final wash, the particles were redispersed in water at a concentration of 10 mg/mL.

2.2.3. Synthesis of magnetic nanorods

Nanorods were assembled by dispersing IONPs in ethanol solution under an external magnetic field. IONPs were synthesized by co-precipitating Fe^{2+} (0.135 M) and Fe^{3+} (0.113 M) salts with aqueous ammonia (400 mL) at 75 °C under vigorous stirring ($pH > 9.5$), as described elsewhere [47]. Briefly, immediately after ammonia addition, ricinoleic acid (10 g) was gradually added over 30 min to hydrophobize the nanocrystals, followed by ageing at 80 °C for 30 min. After cooling, the pH was adjusted to approximately 5 with aqueous nitric acid solution (pH 1) to induce NP flocculation. The precipitate was washed three times with deionized water and methanol, dried, and redispersed in chloroform for storage. Next, deionized water (20 mL) and absolute ethanol (80 mL) were mixed in a beaker placed in a 37 mT magnetic field and stirred at 500 rpm. To initiate the process, 2.5 mL of 25% aqueous ammonia was added, followed by dropwise addition of the nanocrystal suspension into the vigorously stirred mixture. After 5 min, the magnetic field was removed, and TEOS (200 μL) was added dropwise. The mixture was stirred for 30 s and then left undisturbed for 3 h to allow silica condensation. Nanorods were collected by magnetic separation, purified by three ethanol washes followed by three water washes, and finally redispersed in water at a concentration of 10 mg/mL.

2.3. AMP functionalization, AgNP synthesis, and nanorod grafting with AgNPs

All AMP types were first amino-functionalized with APTES to enable subsequent reaction with succinic anhydride, introducing surface carboxyl groups and ensuring good colloidal stability of AMPs in bacterial culture media.

2.3.1. Carboxyl functionalization of AMPs

AMPs (100 mg) were dispersed in a mixture of absolute ethanol (25 mL) and distilled water (25 mL). The suspension was placed in an oil bath maintained at 50 °C. Then, 25% ammonia solution (0.9 mL) was added, followed by APTES (0.3 mL). The reaction mixture was stirred overnight at 50 °C. The next day, the particles were washed twice with distilled water and resuspended in dimethylformamide (20 mL) for further succinic anhydride functionalization. To this AMP suspension, a mixture of additional dimethylformamide (25 mL) and N,N-diisopropylethylamine (0.3 mL) was added. The flask was placed in an oil bath at 50 °C, and then succinic anhydride (200 mg dissolved in 5 mL of dimethylformamide) was introduced. The reaction mixture was stirred at 50 °C for 3 h. After the reaction was complete, the carboxyl-functionalized AMPs were washed with distilled water and resuspended in distilled water to a final concentration of 10 mg/mL.

2.3.2. Synthesis of polyethylene glycol (PEG)-stabilized AgNPs

AgNPs were prepared using a tannic acid reduction method. Briefly, tannic acid (1 mL, 10 mM) was dissolved in ultrapure water (200 mL, 18.2 MΩ·cm), and the pH was adjusted to basic conditions with NaOH. $AgNO_3$ solution (1 mL, 100 mM) was then added under stirring, resulting in the formation of AgNPs. The NPs were stabilized with a PEG-thiol ligand (10 mM). The suspension was purified by centrifugation and dialysis to remove excess reagents before resuspension in ultrapure water or PBS (pH 7.4; 137 mM NaCl, 2.7 mM KCl, 10 mM Na_2HPO_4, and 1.8 mM KH_2PO_4).

2.3.3. AgNP grafting onto nanorods

The surface of the nanorods was first functionalized with APTES as described above. Grafting of AgNPs onto amino-functionalized nanorods was achieved by EDC/NHS coupling, reacting activated COOH groups of PEG-functionalized AgNPs with amines on the amino-functionalized nanorods. AgNPs were dispersed in PBS (pH 7.4) to a final concentration of 0.125 mg/mL. EDC in excess (final concentration: 0.75 μmol/mL) was added and stirred for 10 min. NHS (final concentration: 1.5 μmol/mL, i.e., two equivalents relative to EDC) was then added and stirred for another 10 min. Finally, amino-functionalized nanorods (final concentration: 0.5 mg/mL) were added and stirred for 1 h. The product was purified by magnetic separation, washed three times with ultrapure water, and resuspended in ultrapure water. The calculated silver loading per milligram of nanorods was 17% (w/w).

2.4. Characterization of AMPs and AgNPs

Transmission electron microscopy of NCs, nanorods, and microrods was performed using a Jeol 2100 instrument (Akishima, Japan) equipped with energy-dispersive X-ray spectroscopy (JED 2300 EDS). Samples were prepared by depositing a few drops of the diluted suspension onto 200 mesh TEM grids (SPI Supplies, West Chester, PA) and allowing them to dry. Particle size distributions (n = 200) were determined with ImageJ (version 1.53 t, Java 1.8.0).

The size and shape of AgNPs were determined using TEM (TechNai TEM and Talos L120C). Samples for TEM analyses were prepared by depositing a drop onto ultra-thin carbon-coated copper 200 mesh grids (TED PELLA). A size histogram was created after measuring at least 100 NPs. Imaging of nanorods-AgNPs and nanorods was performed using the same procedure as for AgNPs.

Vibrating sample magnetometry measurements, for magnetic characterization, were conducted at room temperature (VSM 7307, Lake Shore Cryotronics, Westerville, OH) under a maximum applied magnetic field of 10 kOe.

Zeta potential measurements were performed using a Litesizer 500 instrument (Anton Paar, Graz, Austria). NCs and nanorods were diluted to a concentration of 0.025 mg/mL in 10 mM KCl and placed in a beaker for automated titration analysis. The hydrodynamic size, polydispersity, and surface charge of AgNPs were analyzed using a Litesizer 701 dynamic light scattering instrument (Anton Paar) equipped with a 40 mW laser diode operating at a wavelength of 658 nm, along with nanoQ v2.6.4.0 software. The hydrodynamic diameter was measured at an angle of 175 °. All experiments were conducted in triplicate. To assess the surface charge of AgNPs, the samples were diluted in 10 mM NaCl before analysis.

The concentrations of silver ions in AgNPs, and iron ions in microrods, NCs, and nanorods were determined using atomic absorption spectroscopy and PinAAcle 500 PerkinElmer AAS and Syngistix v5.1.0 software. Particles were dissolved in 50% Aqua Regia, and the resulting solution was analyzed by AAS to determine silver and iron ions concentrations.

The colloidal stability of AgNPs was assessed by diluting and incubating them in PBS at 37.4 °C for 1–7 days. The suspensions were then analyzed by UV–Vis and dynamic light scattering analysis. UV–Vis spectra of AgNPs were recorded at 300–800 nm with 0.5 nm steps using a UV-1600PC spectrophotometer (VWR) equipped with M.WAVE Pro 1.0 software.

NP fluorescence was measured in growth medium and buffer using DsRed Express fluorescence settings (excitation at 554 nm and emission at 586 nm) to assess possible NP or AMP-related effects. Low fluorescence was observed in Miller LB medium with NCs. (Fig. S1).

2.5. Bacteria and biofilms

2.5.1. Bacterial cultures

The food isolate *L. innocua* strain ŽM39 [48] from the ZIM Culture Collection (University of Ljubljana) was used. Electrocompetent *L. innocua* ŽM39 cells were prepared as previously described [49]. They were transformed with the vector pJEBAN6 [50], which carries the gene for the reporter protein DsRed Express, by electroporation using the electric pulse generator Vitae (Igea) with two 1 ms pulses at 1.5 kV/cm and a pulse frequency of 1 Hz. Transformed bacteria were selected on media supplemented with erythromycin, and DsRed Express expression was confirmed by fluorescence microscopy. The stock culture was stored at −80 °C and revitalized by culturing on tryptic soy broth (Millipore) agar (VWR) with erythromycin added at a concentration of 10 μg/mL at 37 °C. For overnight culture, *L. innocua* DsRed Express was inoculated into Miller-type lysogeny broth (Sigma-Aldrich) with a pH of 6.8–7.2 and supplemented with 10 μg/mL erythromycin (Miller LB-Ery) and grown at 37 °C and 190 rpm for 16–20 h in an ES-20 orbital shaker (Biosan).

E. faecalis (ATCC 29212, University of Geneva) was cultured from frozen stocks onto Brain Heart Infusion (BHI) agar (Becton Dickinson). Single colonies were transferred into BHI broth (9 mL) and incubated aerobically at 37 °C overnight.

C. albicans (clinical isolate GEGE1122.01, University Hospitals of Geneva) was grown on 4% Sabouraud dextrose agar and subsequently transferred into 4% Sabouraud dextrose broth. Cultures were incubated aerobically at 37 °C overnight.

2.5.2. Growth curve analysis

L. innocua overnight cultures were adjusted to an optical density at 600 nm (OD_{600}) of 0.1 measured in Miller LB-Ery, corresponding to approximately 10^8 colony-forming units (CFU)/mL. AgNPs and SiO_2NPs were diluted in Miller LB-Ery and added to bacterial suspensions at final concentrations of 0.1 and 0.01 mg/mL in final volumes of 200 μL/well. Bacterial cultures were grown in microplates for 24 h at 37 °C with shaking after each cycle of absorbance measurement at 595 nm every 2 min in a microplate reader (Tecan Sunrise). Growth curves were plotted, fitted, and analyzed using QurvE [51,52], and the maximum OD, lag phase, and maximum growth rate were calculated. Maximum OD is determined as the upper asymptote of the fitted growth curve, maximum growth rate is calculated as the maximum slope of the first derivative of the fitted growth curve, and the lag phase is estimated from the intersection of the extrapolated baseline and a tangent at the point of the maximum growth rate. The workflow is illustrated in Fig. S2.

2.5.3. Preparation of titanium grade 4 surfaces for biofilm assays

Commercially pure titanium grade 4 plates (10 × 10 × 1 mm^3) were obtained from Bibus Métal AG (Fehraltorf, Switzerland). The plates were produced by industrial cold rolling (with laminated finish and not mirror-polished) and were accompanied by manufacturer certificates of conformity in compliance with ASTM F67/ISO 5832–2. Handling was performed with nitrile gloves to prevent surface contamination.

Before the experiment, each plate underwent a standardized cleaning sequence. (1) Ultrasonic cleaning in a 3% (v/v) titanium-specific alkaline detergent (Galvex® 17.3%, NGL Cleaning Technology, Switzerland) in deionized water for 10 min. (2) Double rinse in deionized water (2 × 2 min). (3) Rinse in isopropanol ($\geq$ 99.5%) for 2 min. (4) Drying with filtered compressed air (Class 100). After cleaning, the plates were sterilized by saturated-steam autoclaving at 121 °C for 20 min and stored in heat-sealed sterile pouches until use.

2.5.4. Effect of AgNPs on initial adhesion of E. faecalis

E. faecalis overnight cultures were centrifuged (4000 rpm, 5 min) and resuspended in fresh medium. The bacterial density was adjusted to $OD_{600} = 0.5$. For adhesion assays, 200 μL of the bacterial suspension was added to 1.8 mL of fresh medium in 24-well plates containing sterile Ti-G4 plates. AgNPs were added to achieve final concentrations of 0.1, 0.01, 0.001, and 0.0001 mg/mL. Wells were gently mixed before incubation. Samples were incubated for 24 h at 37 °C under aerobic conditions without agitation to allow bacterial adhesion and early biofilm formation.

2.5.5. Biofilm formation

L. innocua overnight cultures, grown for 16–20 h, were adjusted in Miller LB-Ery to $OD_{600} = 0.1$, which resulted in approximately 10^8 CFU/mL of bacteria. These cultures were inoculated into black flat-bottom polystyrene cell culture-treated microtiter plates at 100 μL/well (Nunc, Thermo Fisher). After 1 h of incubation at 37 °C, the supernatant was discarded and replaced with fresh Miller LB-Ery, followed by biofilm growth for 24 h at 37 °C. In the initial adhesion roughly 5 × 10^7 CFU/mL of *L. innocua* bacterial cells adhered to the surface of the well.

Overnight *E. faecalis* and *C. albicans* cultures were centrifuged for 5 min at 4000 × g and 2000 × g, respectively, and their pellets were resuspended in sterile PBS (Gibco, Thermo Fisher Scientific). *E. faecalis* cell density was adjusted to $OD_{600} = 0.5$, corresponding to approximately 2 × 10^9 CFU/mL. Conversely, *C. albicans* cell density was adjusted to $OD_{600} = 0.7$, corresponding to approximately 10^6–10^7 CFU/mL. For biofilm formation, sterile grade 4 titanium plates (10 mm × 10 mm) were placed in 24-well plates, inoculated with either *E. faecalis* or *C. albicans* suspensions, and incubated aerobically at 37 °C for 24 h. After incubation, biofilms were gently washed three times with PBS to remove non-adherent cells.

2.6. *Bacterial adhesion onto AMPs in suspension*

Overnight *L. innocua* cultures were adjusted to $OD_{600} = 0.5$ in Miller LB-Ery. AMPs were stored in 70% ethanol and washed twice with PBS on a magnetic stand (Thermo Fisher) before being resuspended in bacterial suspensions (500 µL) in low-binding microcentrifuge tubes (Corning) at a final concentration of 0.5 mg/mL. To exclude bacteria adhering to the microcentrifuge tube surface, a control without AMPs was included. Samples were incubated for 30 min with agitation at room temperature. Afterwards, the AMPs were magnetically separated on the magnetic stand, and the supernatant was removed. The AMPs were resuspended in Miller LB-Ery and treated in an ultrasound bath (Elmasonic P) at 37 kHz and 30% power for 30 min. After sonication and magnetic separation, serial dilutions were prepared and used for drop plating, performed in triplicate on Tryptic Soy Agar 120 mm plates. Plates with serial dilutions were incubated for 18–20 h at 37 °C. CFUs were counted using OpenCFU software [53].

2.7. *Biofilm treatment and analysis*

2.7.1. *Treatment of L. innocua and E. faecalis biofilms with $AgNO_3$*

$AgNO_3$ was diluted in Miller LB-Ery (for *L. innocua*) and BHI broth (for *E. faecalis)* to final concentrations of 1, 0.1, and 0.01 mg/mL. At 24 h after seeding, *L. innocua* and *E. faecalis* biofilms were washed three times with PBS and then incubated with the corresponding $AgNO_3$ solutions for 24 h at 37 °C. The workflow is illustrated in Fig. S2.

2.7.2. *Treatment of L. innocua, E. faecalis, and C. albicans with AgNPs and SiO_2NPs*

AgNPs and SiO_2NPs were diluted in Miller LB-Ery (for *L. innocua*), BHI broth (for *E. faecalis*), or Sabouraud broth (for *C. albicans*) to final concentrations of 0.1, 0.01, 0.001, and 0.0001 mg/mL (for AgNPs) and 0.1 and 0.01 mg/mL (for SiO_2NPs). At 24 h after seeding, the three different biofilms were washed three times with sterile PBS and then incubated with the corresponding NPs for 30 min or 24 h.

2.7.3. *Magnetic field experimental setups*

Biofilm disruption experiments were performed in 96-well microtiter plates exposed to a rotating magnetic field generated by two different stirring configurations in accordance to the magnetic stirrer used. In case where conventional laboratory stirrer (Hei-PLATE Mix 'n' Heat Core, Heidolph) was used, it was positioned above the microtiter plate (i.e., in an inverted configuration). This configuration was selected to minimize particle sedimentation and reduce magnetic aggregation arising from magnetic field gradients, which is particularly important for larger microrods. For the 96-well plate induction stirrer with 96 stirring positions (MIXdrive 96 MTP, "2 mag" AG, Germany; at 100% power) the 96-well microtiter plate was placed directly on an induction stirrer area. The samples in both configurations were subjected to rotational speeds of 300 or 600 rpm. The data about magnetic field strengths measured in different configurations and conditions are specified in Supporting Material (Fig. S3). A video showing nanoparticle rotation in microtiter wells exposed to the conventional laboratory stirrer is also provided as Supporting Material.

2.7.4. *Treatment of L. innocua with AMPs and nanorod–AgNPs*

AMPs were stored in 70% ethanol and washed twice in PBS on a magnetic stand (Thermo Fisher) before being diluted in Miller LB-Ery to a concentration of 1 mg/mL. The nanorod–AgNPs were stored in water and used directly without a washing step. AgNPs were diluted to a concentration of 0.17 mg/mL, matching the AgNP content in nanorod–AgNPs at 1 mg/mL. At 24 h after seeding, *L. innocua* biofilms were washed three times with sterile PBS before treatment for 30 min at either 300 or 600 rpm on a 96-well induction stirrer. For nanorod–AgNPs, two stirrers at 600 rpm were used: a 96-well induction stirrer and a laboratory stirrer. The experiments with nanorod–AgNPs, nanorods, and AgNPs were conducted either with or without a 24 h incubation at 37 °C after the 30 min treatment. Scheme of the experiment is illustrated in Fig. S2.

2.7.5. *Analysis of biofilm treatment effects*

The efficacy of treating *L. innocua* biofilms was evaluated separately for adhered and dispersed bacteria. After treatment, the dispersed bacteria were removed from the wells and transferred to empty microtiter plate wells. The bacteria that remained adhered were supplemented with fresh medium. For treatments with AMPs and nanorod–AgNPs, the fluorescence of DsRed Express expressed in *L. innocua* was also measured using an M-1000 microplate reader (Tecan) with an excitation wavelength of 554 nm, emission wavelength of 586 nm, 5 nm bandwidth, 3 × 3 reads/well, and 200 flashes. Afterwards, the bacteria were treated in an ultrasound bath (Elmasonic P) at 37 kHz and 30% power for 30 min, the treatment had no significant effect on bacterial viability (Fig. S4). After sonication, serial dilutions were prepared and used for drop plating, which was performed in triplicate on Tryptic Soy Agar 120 mm plates. Plates with serial dilutions were incubated for 18–20 h at 37 °C. CFUs from drops containing 3–30 colonies were counted using OpenCFU software [53].

L. innocua washed biofilms contained approximately 7 log CFU of bacteria. In experiments we used biofilms with a monolayer of firmly adhered *L. innocua* cells 24 h after seeding (Fig. S5). Using fluorescence-based detection of DsRed Express in untreated bacteria (log 7), we obtained 400–700 relative fluorescence units, which is relatively low but still clearly above the detection limit. For dispersed bacteria, the fluorescence signal dropped below the detection limit, and thus viability assays were used. By contrast, the remaining adhered bacteria were evaluated using both fluorescence-based detection and viability assays.

After treatment, *E. faecalis* and *C. albicans* biofilms were washed three times with PBS and transferred to fresh tubes containing PBS. Biofilm cells were detached by vortexing for 2 min followed by sonication for 20 s. Suspensions were serially diluted, plated on BHI agar (for *E. faecalis*) and Sabouraud agar (for *C. albicans*), and incubated for 24 h at 37 °C. CFUs were counted from plates containing 20–300 colonies. Each condition was tested in triplicate and repeated in three independent experiments (n = 9). The workflow is illustrated in Fig. S2.

2.7.6. *Scanning electron microscopy (SEM) of samples containing AMPs, AgNPs, and bacteria*

L. innocua biofilms were grown on black, polystyrene, cell culture-treated microtiter plates (Nunc) for 24 h. The biofilms were washed three times with PBS and treated with 0.17 mg/mL AgNPs, 1 mg/mL nanorods, and 1 mg/mL nanorod–AgNPs (prepared in PBS) for 30 min at 600 rpm using a laboratory stirrer. After treatment, biofilms were fixed with 2.5% glutaraldehyde in PBS buffer for 30 min, washed in PBS (2 × 5 min), and washed in distilled water (2 × 30 s). Samples were dehydrated using a graded ethanol series (30%, 50%, 70%, and 90%) and incubated for 5 min at each step. Finally, the samples were incubated twice for 5 min in absolute ethanol, frozen in liquid nitrogen, and dried overnight by lyophilization. After lyophilization, the samples were sputter-coated with a 5 nm Au/Pd (80/20) layer at 10 mA for imaging. SEM was performed on a Verios 4 G HP microscope (Thermo Fisher), and bacterial lengths (n = 300/sample) were measured using ImageJ software.

2.8. Statistical analysis

All experiments were conducted in three independent biological replicates, each with three technical repeats, except for SEM, for which only three independent biological replicates were performed. For *L. innocua*, we calculated the bacterial concentration from the CFUs for each replicate. The log reduction was determined as the base-10 logarithm of the ratio between the mean CFU concentrations of the untreated controls and treated samples. Statistical analysis was conducted on normalized relative fluorescence units, $\log_{10}$ reductions of bacterial concentrations, growth curve analysis parameters, and normalized bacterial lengths. For data illustration, CFU or $\log_{10}$ reduction was used. For growth curve analysis, nonparametric fitting was conducted in QurvE [51,52], and maximum OD, lag phase, and growth rate were calculated.

For *E. faecalis* and *C. albicans* assays, CFU data were $\log_{10}$-transformed before statistical testing.

Normality of the data was assessed using the Shapiro–Wilk test. If normality was met, we used ordinary ANOVA with Dunnett's multiple comparison tests. When normality was not met, Kruskal–Wallis tests with Dunn's multiple comparisons correction were applied. Statistical analyses were performed using GraphPad Prism (version 10.4 or 10.6), with $p < 0.05$ considered significant.

3. Results and discussion

In this study, we investigated the potential of magneto-mechanical disruption as a strategy for biofilm removal using persistent *L. innocua* biofilms as a model system. We systematically assessed the effects of a range of AMP properties, including surface roughness, size, and magnetic responsiveness on biofilm removal under various magnetic field settings. The most effective AMPs were then functionalized by grafting AgNPs, enabling evaluation of both mechanical disruption and localized antibacterial action under rotating magnetic field actuation. This revealed a synergistic effect on biofilm removal and inactivation. To place these findings in a broader biological context, additional comparative assays with AgNPs were performed on *E. faecalis* and *C. albicans* biofilms, demonstrating that the efficacy of AgNPs is species-dependent. Altogether, our findings highlight the broad versatility of the proposed hybrid strategy across different biofilm-forming microorganisms.

3.1. *L. innocua* biofilm removal by NCs with differently rough surfaces

The first AMPs to be assessed were NCs with distinct silica shell roughness. These nanomaterials were fully characterized in our previous work, which demonstrated antibacterial efficacy against the biofilms of Gram-negative *Escherichia coli* and *Pseudomonas fragi* and Gram-positive *Lactococcus lactis* [33]. Building on these findings, we tested the same silica-coated NCs on *L. innocua* biofilms, which form relatively non-extensive structures with firmly adhered bacteria in the basal layers and minimal EPS. We investigated whether increased surface roughness of NCs improves antibiofilm efficacy under rotating magnetic fields.

We assembled spherical NP clusters into NCs (882 ± 255 nm in length and 193 ± 26 nm in width, with mean aspect ratio of 4.6, Fig. S7A), which were then coated with silica of varying roughness (Fig. 1). Increased AMP roughness can increase effective surface area and transmit stronger mechanical forces due to sharper edges compared to smooth surfaces, potentially affecting the efficacy of removing persistent *L. innocua* biofilms. Furthermore, the silica shell on the AMP surface has a hardness in the gigapascal range [54,55], whereas biofilms are generally soft, viscoelastic materials with mechanical properties in the kilopascal range [56]. This substantial mechanical contrast likely allows the rigid silica-coated AMP to impose localized stresses on the much softer biofilm matrix during actuation, promoting structural disruption and facilitating biofilm detachment.

To improve colloidal stability, we functionalized the particles with carboxyl groups to decrease direct bacterial adhesion and promote uniform dispersion within biofilms. Zeta potential analysis confirmed

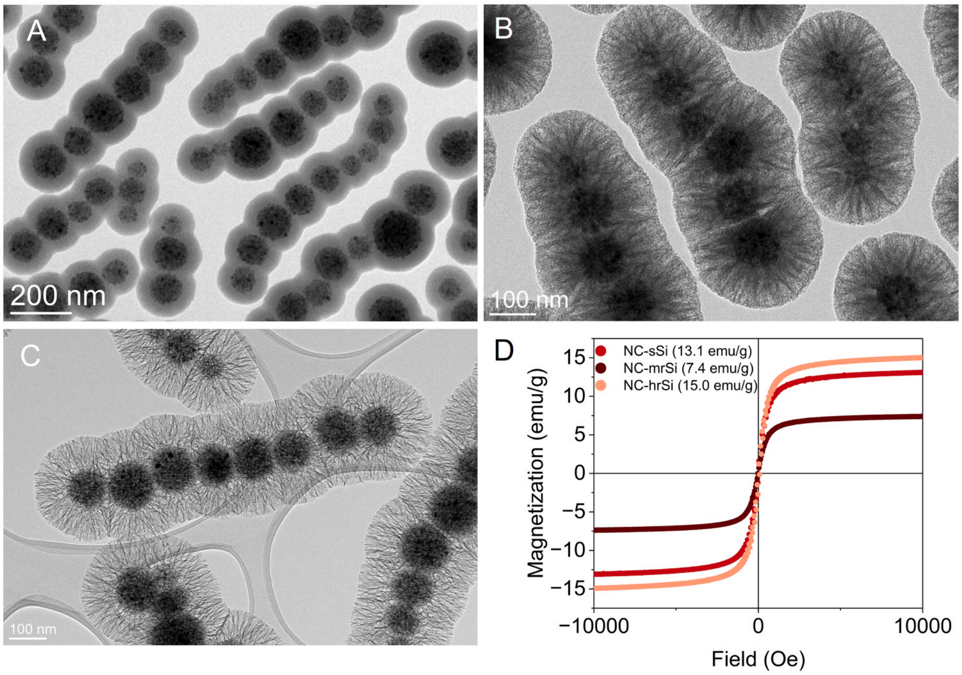

Fig. 1. Silica-coated nanochains with varying surface roughness. (A) Smooth (NC-sSi), (B) moderately rough (NC-mrSi), and (C) highly rough (NC-hrSi) nanochains. (D) Vibrating sample magnetometry measurements of the nanochains at room temperature.

successful surface modification, as the isoelectric point shifted from approximately pH 10 (amine functional groups) to pH 3.5. Owing to their elongated shape and strong magnetic responsiveness, NCs can align and rotate under an external magnetic field and are therefore expected to exert mechanical forces within biofilms. Vibrating sample magnetometry verified their superparamagnetic properties (absence of hysteresis), with saturation magnetization decreasing after silica coating, with values of 13.1, 7.4, and 15.0 emu/g for NC-sSi, NC-mrSi, and NC-hrSi, respectively (Fig. 1D). This decrease reflects the contribution of diamagnetic silica, which increases the composite mass without adding to its magnetic moment. Nonetheless, all NC types retained stable superparamagnetic properties (Fig. 1D).

Biofilms in microtiter plate wells were treated with NCs in a magnetic field generated by a 96-well induction stirrer, which initiated NC rotation at two speeds (300 and 600 rpm). Both the CFU- and fluorescence-based results showed no differences in antibiofilm efficacy among the NCs with varying surface roughness or compared to the control (Figs. 2A, B, S6A).

The lack of any effect is inconsistent with previous findings using NCs for the removal of biofilms of different bacterial species: *E. coli*, *P. fragi*, and *L. lactis* [33]. In this previous study, NCs exhibited a biofilm removal efficacy rate of approximately 90%, corresponding to an approximately 1 $\log_{10}$ reduction for Gram-negative *E. coli* and *P. fragi* and a 0.5 $\log_{10}$ reduction for Gram-positive *L. lactis*. However, these effects did not depend on surface roughness. In addition, similar AMPs damaged a *Staphylococcus epidermidis* floating biofilm, making bacteria accessible to methicillin, especially when swarm-forming AMPs were used [25]. However, such swarm formation was not observed in our experiments. This difference may be attributed to the relatively weak magnetic field generated by the 96-well induction stirrer, which was approximately 10-fold lower than in the previous study [25] and may have not enabled the anisotropic chains to align into coordinated, swarm-like assemblies. Furthermore, the observed species-specific effects suggest that differences in biofilm characteristics may influence the antibiofilm efficacy of NCs.

Importantly, *Listeria* biofilms exhibit strong surface adhesion [57], and their interactions with abiotic surfaces are electrostatic [58]. Teichoic acids are decorated with neutral sugars but have an overall negative charge due to their phosphate groups. Altogether, they contribute to hydrophilicity, attract cations, and enable hydrogen bonding. Adhesion is also mediated by proteins present on the surface of *Listeria* cells [58–60]. *L. innocua* biofilms were cultured on tissue-culture-treated polystyrene microtiter plates with negatively charged and hydrophilic surfaces, which facilitate protein adsorption and bacterial attachment. Our results show that *L. innocua* biofilms comprised a monolayer of bacterial cells that firmly adhered to the polystyrene surface (Fig. S5A).

Listeria biofilms also lack the soft, thick layer of EPS (Fig. S5A) that is present in *S. epidermidis* biofilms [25]. In conclusion, the lack of any antibiofilm effect of NCs was attributed to the characteristics of *L. innocua* biofilms (i.e., firmly adhered bacterial cells and the absence of sticky EPS) and the relatively small size of NCs, which generate forces too weak for the removal of *L. innocua* biofilms. These findings motivated further investigation into the antibiofilm efficacy of larger AMPs, as also suggested by Šavli et al. [33].

3.2. *L. innocua biofilm removal by AMPs of different sizes*

Next, we investigated whether larger AMPs, when exposed to a rotating magnetic field, could induce stronger antibiofilm effects. In addition to the NCs described above, two additional types of AMPs were designed, synthesized, and evaluated for their effects on biofilm dispersal: microrods and nanorods (Figs. 3 and 4). These AMPs were purposefully designed with distinct shapes, lengths, and aspect ratios to enable direct comparisons of how geometry governs their ability to interact with and mechanically perturb biofilms in rotating magnetic fields.

Nanorods were prepared from hydrophobic IONPs with a saturation

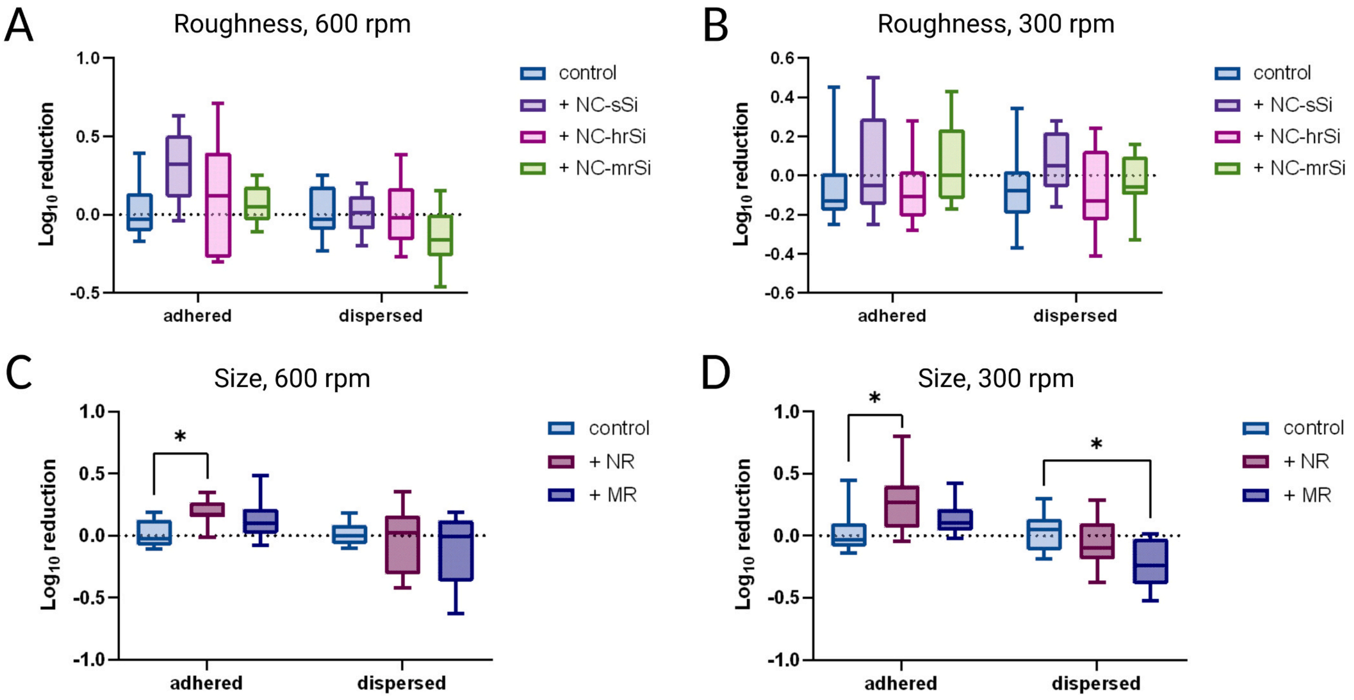

Fig. 2. $\log_{10}$ reduction of biofilm bacterial colony-forming units (CFUs) after treatment with anisotropic magnetic particles (AMPs) of varying roughness and sizes. Adhered and dispersed bacteria CFUs were counted after treatment of biofilms with nanochains (1 mg/mL) with different surface roughness: smooth (NC-sSi), moderately rough (NC-mrSi), and highly rough (NC-hrSi). Biofilms were treated for 30 min at 600 rpm (A) and 300 rpm (B). Biofilms were also treated with AMPs (1 mg/mL) of different sizes (nanorods (NRs) and microrods (MR)) for 30 min at 600 rpm (C) and 300 rpm (D). Error bars denote min and max ranges. ANOVA with Dunnett’s tests revealed significance levels of $p < 0.05$ (*).

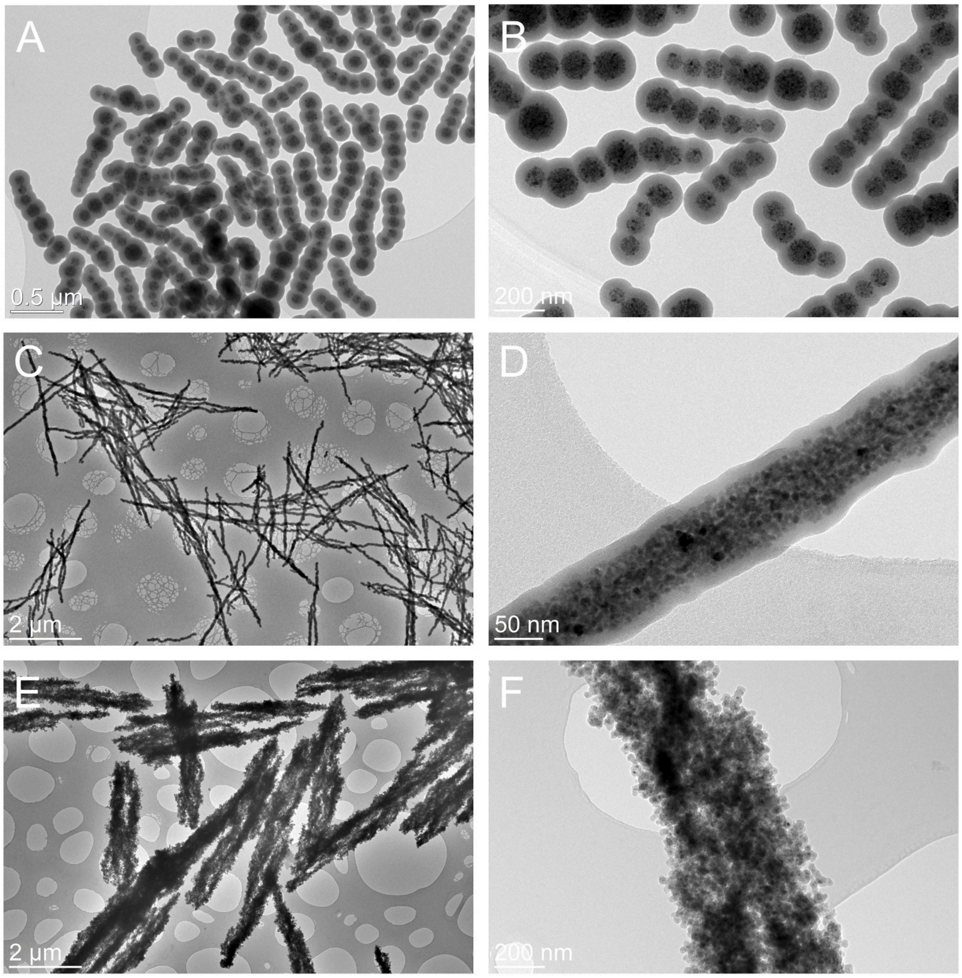

Fig. 3. Representative transmission electron microscopy images of nanoparticles. (A, B) Smooth nanochains, (C, D) nanorods, and (E, F) microrods.

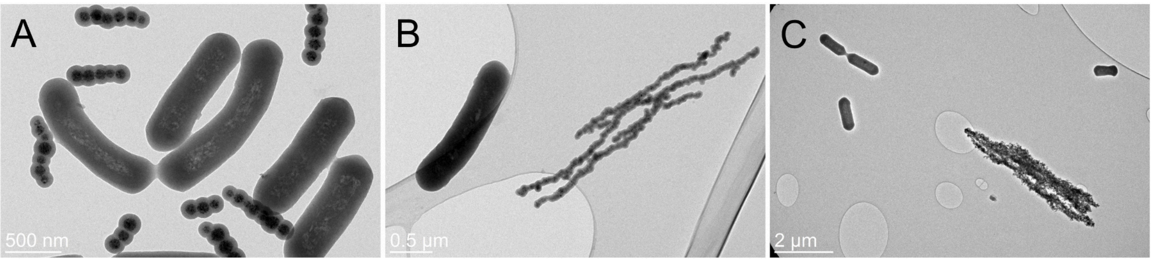

Fig. 4. Representative transmission electron microscopy images of particles in presence of *L. innocua.* (A) Smooth nanochains, (B) nanorods, and (C) microrods.

magnetization of 48.8 emu/g. Dispersing nanocrystals in a suspension under a 37 mT magnetic field aligned the assembled structures into anisotropic nanorods with a mean length of 1.9 ± 0.7 µm and 94 ± 13 nm width (mean aspect ratio of 20) (Fig. S7B). Subsequent silica coating decreased the saturation magnetization to 15.4 emu/g (Fig. S7D).

Microrods were synthesized by magnetically assembling numerous citric acid-stabilized IONPs that had been colloidally destabilized by increased ionic strength and have an average length of 12.6 ± 5.2 µm and width of 0.6 ± 0.2 µm (mean aspect ratio of 21) (Fig. S7C). To mechanically stabilize their structure, a thin silica layer was deposited, which enhanced colloidal stability and enabled further functionalization. This silica coating decreased the saturation magnetization of citric acid-stabilized IONPs from 55.7 to 33.9 emu/g, consistent with the additional diamagnetic silica mass. However, these microrods still exhibited superior magnetic responsiveness in translational movement due to their large volume (Fig. S7D). TEM analyses confirmed that microrods had the thinnest silica layer among the three AMP types (Fig. 3), thereby retaining comparatively high magnetization relative to nanorods and NCs. All three AMP types were functionalized with APTES and succinic anhydride to introduce carboxyl groups, ensuring colloidal stability, decreasing bacterial adhesion, and enabling effective dispersion within biofilms.

L. innocua biofilms were treated as in the first experiment with NCs to evaluate the effects of AMPs with the same smooth silica coating but different particle sizes (NC-sSi, nanorods, and microrods). During the experiments, we observed that microrods were partially deposited on the bottoms of the wells during treatment, due to their large size compared to NCs and nanorods. Microrods tended to sediment spontaneously and relatively quickly, which was more pronounced at the lower rotational speed. The mixing speed influenced microrods dynamics, as the higher mixing speeds (600 rpm) seems to generate more efficient motion compared to lower speed (300 rpm).

Overall, at both rotational speeds, significant differences in CFU counts were observed for selected AMP treatments of different sizes compared to the untreated control (Fig. 2). Specifically, nanorods showed significant effects in the adhered biofilm fraction at both 300 rpm ($p = 0.0254$) and 600 rpm ($p = 0.0152$), whereas microrods exhibited a significant decrease only in the dispersed biofilm fraction at 300 rpm ($p = 0.0162$) (Fig. 2C, D). By contrast, fluorescence measurements of the treated biofilms showed a significant decrease only for microrods at 600 rpm in the adhered fraction ($p = 0.0102$) (Fig. S6B). When comparing the efficacy of nanorods, microrods, and NCs at 600 rpm, nanorods and NCs exhibited significant $\log_{10}$ reduction values of approximately 0.3 ($p = 0.0005$) and 0.2 ($p = 0.0424$), respectively, thereby exhibiting significant antibiofilm effects. At 300 rpm, nanorods reached a $\log_{10}$ reduction of 0.3 ($p = 0.0069$). Microrods produced only a limited $\log_{10}$ reduction of 0.1 (Fig. S8). Therefore, nanorods showed the most consistent effect on the adhered biofilm fraction, reaching a 0.2–0.3 $\log_{10}$ reduction corresponding to approximately 37% and 50% decreases, respectively.

The lower efficacy of microrods is likely associated with their reduced dispersal stability during actuation, as their relatively large size prevents true colloidal behavior. Efficient biofilm disruption requires particles to remain well dispersed in suspension, enabling sustained rotational motion and repeated interactions with the biofilm matrix. Although vibrating sample magnetometry measurements indicated that microrods possess the highest magnetization and thus a strong magnetic response, their large size increases the tendency to sediment, which likely limits their effective motion at the biofilm interface under the applied magnetic field conditions. These observations indicate that antibiofilm performance is not governed solely by the intrinsic magnetic properties of the particles, but rather by a complex interplay between magnetic actuation parameters, particle mobility, size and shape, magnetic moment, biofilm characteristics, and suspension stability. Notably, nanochains and nanorods exhibit comparable saturation magnetization values and similar effective magnetic moments per particle, as the magnetic volume is comparable (nanorods are approximately twice longer than nanochains but significantly narrower). Furthermore, both systems display similar colloidal stability. Therefore, the superior biofilm removal performance of nanorods is likely related to their smaller cross-sectional diameter. This feature may enhance their ability to interact mechanically with soft biological matter, facilitating more efficient disruption of the biofilm matrix. Overall, these results suggest that nanorods achieve the most favorable balance among the governing parameters, leading to the most effective biofilm disruption under the tested conditions.

Comparable studies have shown that particle size, shape, and field conditions govern magneto-mechanical biofilm removal, supporting the credibility of our results regarding nanorods [25,33]. Particle sizes range from hundreds of nanometers to micrometers, achieving varying levels of biofilm removal. For example, Fe_3O_4-loaded polydopamine hollow rods (393 × 121 nm) decreased *Staphylococcus aureus* biofilm biomass by approximately 10% after 10 min of exposure to rotating magnetic fields (2000 rpm) and by 53.0 ± 7.2% after 15 min [61]. Bhuyan et al. [62] synthesized larger anisotropic particles (50–160 μm), achieving decreases in *S. aureus* and *Pseudomonas aeruginosa* viability by 77% and 74.2%, respectively, under unidirectional motion (10 mT, 8 kA/m, 8 s of actuation), with further decreases under spinning motion (by 76.1% and 79.2%). Mayorga-Martinez et al. [63] reported 400 nm halloysite nanotube-based nanorobots coated with polyethyleneimine for ampicillin loading, which, under magnetic actuation (10 Hz, 5 mT, 4 kA/m, 1 h), penetrated *S. aureus* biofilms on titanium mesh and achieved a 93% decrease. However, biofilm removal was suboptimal in all these cases, ranging from a 0.25 $\log_{10}$ reduction (corresponding to 40% removed biofilm) up to a 0.7 $\log_{10}$ reduction (80% removed biofilm) and 1.1 $\log_{10}$ reduction (93% removed biofilm). It is important to note that there is considerable variability in particle characteristics, biofilm species-dependent mechanical properties, magnetic fields, exposure times, assay conditions, and microbiological tests, all of which contribute to differences across studies.

Many previous reports have indicated that larger anisotropic assemblies correlate with stronger biofilm disruption [25,31,62]. However, our current findings show that larger particles (microrods, which are too large to be colloidal) exhibit poor physical stability, limited mobility, and lower antibiofilm efficacy compared to smaller, colloidal NPs (nanochains and nanorods). This discrepancy may be explained by the following mechanism of sequential disruption. In some systems, smaller particles initiate early biofilm penetration. Afterwards, larger, sufficiently stable assemblies, which are formed from smaller NPs (such as the nanorods used in this study) cause more extensive damage during prolonged exposure, accounting for the higher efficacies reported.

In our previous work, magnetic NCs formed spinning swarms (~17 μm) under a low-frequency rotating magnetic field (~10 rpm, ~15–20 mT, 24 h) and enhanced antibiotic efficacy against floating *S. epidermidis* biofilms, resulting in a 4 $\log_{10}$ reduction in methicillin-resistant strains [25]. Furthermore, in a study conducted under different magnetic field exposure conditions, using the same microrods, these particles outperformed smaller AMPs [64]. This behavior was attributed to the fact that elongated magnetic particles experience a torque (τ) proportional to their magnetic moment (μ) and the applied magnetic field (B): $\tau = \mu \times B$. Because of their larger volume, microrods have a significantly higher magnetic moment, which, combined with their relatively high saturation magnetization (33.9 emu/g compared to 13–15 emu/g for nanochains and nanorods), results in substantially greater torque generation than that of nanoscale AMPs. Notably, nanorods have an aspect ratio comparable to that of microrods, suggesting that particle anisotropy alone does not fully explain the observed differences in performance. Instead, these findings support the conclusion that biofilm disruption efficiency results from a complex interplay of multiple parameters, rather than from a single dominant physical property. Overall, the contrasting performance of microrods across studies indicates that magnetic field exposure conditions play a critical role in determining their effectiveness, in addition to the intrinsic physical characteristics of the biofilm.

3.2.1. *Planktonic L. innocua adheres to AMPs*

To assess potential interactions between bacteria and AMPs that could affect the observed antibiofilm effects, the adhesion of *L. innocua* planktonic cells to AMPs of various sizes and surface roughness was evaluated after 30 min. For all AMPs, CFU counts were in the range of 10^8 CFU/mL. Regarding surface roughness, bacteria adhered least to NC-mrSi, whereas the differences between NC-sSi and NC-hrSi were minimal. Log_{10} reduction values indicating bacteria adhered to the AMPs were all highly significant compared to the control: approximately 0.7 for NC-sSi ($SD = 0.12$, $p < 0.0001$), 0.5 for NC-mrSi ($SD = 0.19$, $p < 0.0001$), and 0.6 for NC-hrSi ($SD = 0.19$, $p < 0.0001$) (Fig. S9). Regarding size, NCs (0.7 for NC-sSi, $SD = 0.1$, $p < 0.0001$) and nanorods (0.7, $SD = 0.2$, $p < 0.0001$) exhibited the highest $\log_{10}$ reduction values, whereas significantly fewer cells adhered to microrods (0.4, $SD = 0.3$, $p = 0.0014$) compared to the control without particles (Fig. S9). This observation can be attributed to the greater total surface area of smaller AMPs at the same mass concentration, which provides more available sites for bacterial attachment.

After 30 min of exposure, substantial bacterial adhesion occurred on all AMP surfaces. No clear trend was observed between AMP surface roughness and bacterial adhesion. All AMPs had carboxyl groups exposed on their surfaces, which confer a negative charge. This enables interactions with cell-surface proteins and teichoic acids and thus favors the adhesion of *Listeria* [58,59]. Adhesion of planktonic bacteria is non-negligible, therefore these AMPs likely adhere to or become entrapped within the biofilm.

3.3. Hybrid approach to biofilm removal by nanorod–AgNPs

Many successful approaches have combined magneto-mechanical disruption with an additional antibacterial modality, such as antibiotics [25], photothermal therapy [65], and reactive oxygen species [66]. Following this rationale, we grafted AgNPs onto nanorods, thereby combining magneto-mechanical action with a complementary bactericidal effect. Although NCs and nanorods exhibited comparable effects on *L. innocua* biofilms, nanorods were selected because they are larger than *L. innocua* bacterial cells (~ 1 µm), remain well-dispersed in media, have greater potential for biofilm removal through the generation of stronger mechanical stirring forces, and are easy to produce. In the proposed hybrid magneto–chemical system, anisotropic magnetic nanorods disrupt biofilms through rotational motion, whereas AgNPs directly affect bacteria in biofilms. We first analyzed the effects of AgNPs in our model bacterial systems and then used *L. innocua* model for the hybrid approach.

3.3.1. The effects of AgNPs on planktonic and biofilm bacteria

AgNPs were synthesized by reducing silver ions with tannic acid [67]. To enhance stability and facilitate effective grafting of AgNPs onto nanorods functionalized with APTES, AgNPs were further functionalized with carboxylic acid-modified PEG via a thiol-silver linkage. The PEGylated AgNPs demonstrated good colloidal stability in PBS, as confirmed by UV–Vis and dynamic light scattering analyses (Fig. S10A, B). TEM analysis showed a mean particle diameter of 12.1 ± 0.9 nm (Fig. 5A), whereas dynamic light scattering measurements indicated a mean hydrodynamic diameter of 13.8 ± 1.1 nm with a polydispersity index of 0.11 ± 0.02. Zeta potential analysis showed a surface charge of −42.9 mV. Nanorod–AgNPs were prepared by conjugating AgNPs to nanorods functionalized with APTES via EDC/NHS coupling, with successful grafting confirmed by both TEM imaging (Fig. 5B, C) and UV–Vis spectroscopy (Fig. S10C).

Before the combined magneto-chemical treatment, species-dependent variability was assessed by characterizing the bioactivity of AgNPs using *L. innocua, E. faecalis*, and *C. albicans*. First, we assessed the toxicity of AgNPs against *L. innocua* by monitoring planktonic bacterial growth curves in the presence of different AgNP concentrations and comparing them with those obtained using SiO_2NPs at the same concentrations (Fig. S11), which served as a control to determine whether the mere presence of assumedly inert nanoparticles affect bacterial growth. At the highest AgNP concentration (0.1 mg/mL), bacterial growth was much lower than that in the control or with 0.1 mg/mL SiO_2NPs ($p < 0.0001$), despite a relatively high standard deviation (Fig. S11A). Maximum OD after 24 h and maximum growth rate was also significantly lower in the presence of 0.1 mg/mL AgNPs compared to the control ($p = 0.0016$), whereas lag time showed no significant differences; both parameters also exhibited high standard deviations (Fig. S11B, C, D). Furthermore, viability was determined by CFU counts of planktonic *L. innocua* after 24 h of growth in the presence of AgNPs. The results showed a significant ($p = 0.0006$) mean $\log_{10}$ reduction of 4.4, but with a high standard deviation of 1.8 (Fig. S11E). In summary, a low AgNP concentration (0.01 mg/mL) was not toxic to *L. innocua*, whereas a higher concentration (0.1 mg/mL) significantly decreased the growth rate and maximum OD of planktonic bacteria, achieving an antibacterial effect after 24 h (Fig. S11). High variability in the effects of AgNPs was consistently observed in experiments with planktonic *L. innocua*.

Next, we tested the effects of AgNPs on *L. innocua* biofilms. After 30 min of incubation with AgNPs, no significant changes in biofilms were observed in the adhered or dispersed bacterial fractions compared to the untreated control or SiO_2NP-treated biofilms. However, 0.1 mg/mL SiO_2NPs produced significantly greater biofilm growth ($p = 0.0384$) compared to the untreated control in both the adhered biofilm and dispersed fraction ($p = 0.0478$) (Fig. S12A), likely by providing an additional surface area for adhesion and growth. Bacteria in biofilms are altered and more resistant to the environment, and thus the lack of any effect of AgNPs after 30 min of exposure was expected. To further assess potential time-dependent effects, biofilm exposure was prolonged to 24 h. Significantly greater growth compared to untreated control of adhered bacteria was observed with SiO_2NPs ($p = 0.0034$ and < 0.0001) and 0.01 mg/mL AgNPs ($p = 0.0361$). No significant differences were observed in the dispersed bacterial fraction (Fig. S12B). Prolonged AgNP exposure mostly increased the variability of the CFU measurements rather than producing consistent antibiofilm effects.

To evaluate the sensitivity of *L. innocua* biofilms to Ag^+ ions, biofilms were treated with 1, 0.1, and 0.01 mg/mL $AgNO_3$ for 24 h. AgCl precipitates formed upon addition of $AgNO_3$ to the medium, making it impossible to determine the exact effective concentration. Nevertheless, high sensitivity to Ag^+ ions was observed. For all three concentrations, significant CFU decreases in biofilms exposed to $AgNO_3$ were observed in both the adhered ($p < 0.0001$) and dispersed ($p < 0.0001$, < 0.0001, and $= 0.0006$) bacterial fractions compared to the untreated control (Fig. S12C). Overall, all $AgNO_3$ concentrations showed high toxicity against *L. innocua* biofilms.

Previous experiments with AgNPs of 20–40 nm in size revealed minimal inhibitory concentration values between 3.125 µg/mL and 0.010 mg/mL and minimal bactericidal concentration values around 0.020 mg/mL [68,69]. These studies used concentrations lower than those used in our experiments, matching only our lowest AgNP concentration of 0.01 mg/mL.

To evaluate the generalizability of the observed effects of AgNPs, additional assays were performed on resilient Gram-positive *E. faecalis* and *C. albicans* yeast. Both these species are part of human microbiota but can act as opportunistic pathogens [70,71]. First, mature (24 h) *E. faecalis* and *C. albicans* biofilms were exposed for 24 h to 0.0001–0.1 mg/mL AgNPs. Neither *E. faecalis* nor *C. albicans* biofilms showed any significant decreases in CFU counts at any AgNP concentration (Fig. S13A, B). These findings are consistent with the known tolerance of fungal biofilms to NP-based treatments [72].

Next, *E. faecalis* was evaluated during early stages of biofilm formation (initial adhesion) under identical AgNP exposure conditions. After 24 h of treatment, no measurable inhibitory effects were observed, and CFU counts remained comparable to those of untreated controls

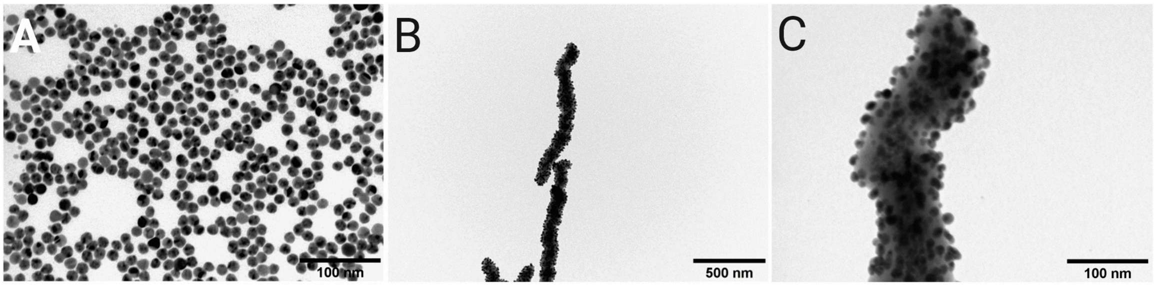

Fig. 5. Representative transmission electron microscopy images of silver nanoparticles. (A) AgNPs and (B, C) nanorod–AgNPs.

(Fig. S14).

To determine whether Ag^+ ions could overcome this tolerance, *E. faecalis* biofilms were treated with aqueous $AgNO_3$ at 1, 0.1, and 0.01 mg/mL. No decreases in viable cells were observed at any $AgNO_3$ concentration (Fig. S15), confirming that *E. faecalis* biofilms are highly resilient to both NPs and Ag^+ ions. These results are consistent with previous findings showing that *E. faecalis* retains structural integrity and metabolic activity despite exposure to conventional disinfectants [70,73]. Similarly, during the initial adhesion phase, *E. faecalis* showed no inhibition and even a modest increase in viable counts at the highest NP concentration (Fig. S14). Overall, the data underscore that silver-based treatments cannot be assumed to be universally effective and support the need for hybrid magneto–chemical strategies that account for microbial physiology, biofilm architecture, and experimental context.

Previous studies have shown that the effects of AgNPs depend on the particle's size, shape, surface coating, and synthesis method as well as the microorganisms used. Data on the specific nature of AgNPs used in microbiological studies are inconsistently reported or not readily accessible, making meaningful comparisons across studies difficult. It has been reported that spherical AgNPs have the best antibacterial properties because of their maximal surface area for bacterial exposure. Surface coating is important for the stability of AgNPs, influencing their antimicrobial effect and improving their biocompatibility with mammalian cells [36,74–76]. The size of AgNPs also influences their antimicrobial effects. AgNPs measuring less than 10 nm or even 20 nm can penetrate bacterial cells, rupturing the cell wall and increasing cell permeability. This has harmful consequences in bacteria, including effects on DNA replication, protein synthesis, cell wall synthesis, protein denaturation, generation of reactive oxygen species, and disruption of the cell's electrochemical potential.

In addition to the effects mentioned above, AgNPs that release Ag^+ ions exert effects related to the binding of silver to all negatively charged molecules in the bacterial cell. Whether a substantial part of AgNP toxicity originates from Ag^+ ions has not yet been fully resolved [75]. It is also important to note that Gram-negative bacteria are usually more susceptible to the antimicrobial effects of AgNPs than Gram-positive bacteria because of their thinner cell wall [74,77]. The AgNPs used in this study were coated with PEG to increase their colloidal stability [76,78]. They had a mean hydrodynamic diameter of 13.8 ± 1.1 nm, which did not decrease significantly over a week (Fig. S10A), indicating negligible release of Ag^+ ions under the tested conditions. However, this may depend on the incubation medium and time. *L. innocua* and *E. faecalis* are Gram-positive bacteria with thick cell walls and are therefore less susceptible to particle penetration [74]. Given the characteristics of AgNPs, their mode of action is probably through contact with the bacterial cell wall.

Collectively, these findings demonstrate that silver-based chemical treatments alone are insufficient to eradicate mature and resistant biofilms, such as those formed by *L. innocua, E. faecalis,* and *C. albicans*. This supports the design of a hybrid mechano-chemical strategy.

3.3.2. *Combined mechano-chemical biofilm removal using hybrid nanorod–AgNPs*

To evaluate a hybrid magneto–chemical strategy, AgNP-grafted nanorods were tested against *L. innocua* biofilms and compared to untreated controls, AgNP-only treatments, and nanorod-only treatments (Fig. 6). Based on the results of the antibacterial assessment of AgNPs on *L. innocua* biofilm, we hypothesized that AgNPs alone would not affect *L. innocua* biofilms within 30 min. Therefore, nanorods were used to disrupt biofilms, thereby facilitating bacterial exposure to hybrid nanorod–AgNPs and enabling a synergistic effect.

The concentration of AgNPs was adjusted to match the silver content in the nanorod–AgNPs at 1 mg/mL. *L. innocua* biofilms were treated in a magnetic field at 600 rpm, a speed previously shown to provide better AMP colloidal stability and even dispersion throughout the microtiter well. The magnetic fields were applied using both a 96-well induction

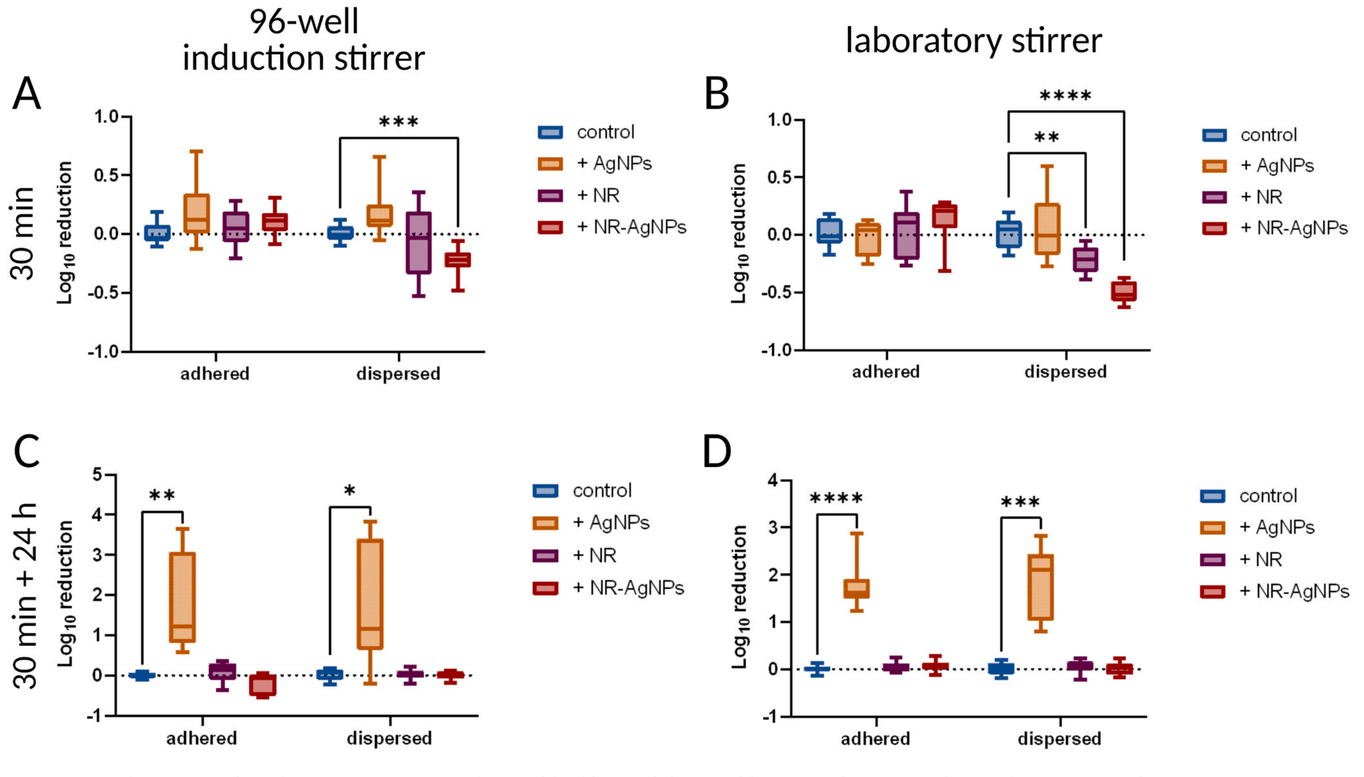

Fig. 6. Log_{10} reduction in colony-forming units (CFUs) of treated biofilms and dispersed bacteria. The untreated control was compared to 30 min treatments with silver nanoparticles (AgNPs) (0.17 mg/mL), nanorods (NRs) (1 mg/mL), and nanorod–AgNPs (NR–AgNPs) (1 mg/mL) with different stirrers and incubations. Samples were treated on either a 96-well induction stirrer (A, C) or laboratory stirrer (B, D) without further incubation (A, B) or with an additional 24 h of incubation (C, D). Error bars denote min and max ranges. ANOVA revealed significance levels of $p < 0.05$ (*), $p < 0.01$ (**), $p < 0.001$ (***), and $p < 0.0001$ (****).

stirrer and a laboratory stirrer. The laboratory stirrer was introduced because the magnetic field strength of the 96-well induction stirrer was limited to a maximum of approximately 2 mT (Fig. S3), whereas the laboratory stirrer in the inverted configuration (described in the Methods section) achieved field strengths of up to approximately 10 mT (Fig. S3). The synergistic effects of nanorods and AgNPs were observed with both stirrers, but were more pronounced with the laboratory stirrer. Compared to the untreated control, a significant reduction of approximately 0.5 $\log_{10}$ (Fig. 6A, B) was achieved with the 96-well induction stirrer ($p = 0.0007$) and the laboratory stirrer ($p < 0.0001$) in the dispersed but not adhered bacterial fraction. This indicates that nanorod rotation in the rotating magnetic field helps NPs interact with biofilms, resulting in synergistic effects of hybrid magneto–chemical biofilm disruption. The antibiofilm effects of AgNPs alone varied considerably between experiments, reaching a mean $\log_{10}$ reduction of 0.2 ± 0.3. In addition, fluorescence intensity measurements did not show any significant differences in biofilms after 30 min of treatment, limiting their usefulness in such settings (Fig. S6C).

Next, the effects of prolonged exposure of *L. innocua* biofilms to nanorod–AgNPs were assessed. Antibiofilm effects of AgNPs on *Staphylococcus pseudintermedius* have been demonstrated after 24 h [79]. Additionally, the effects of 0.1 mg/mL AgNPs on *L. innocua* planktonic bacteria were more pronounced after 24 h. Therefore, we tested whether this effect also applies to treated biofilm by adding a 24 h regrowth period in the presence of AgNPs and nanorod–AgNPs after the 30 min magnetic stirring treatment. The antibiofilm effects of AgNPs alone at a similar concentration of 0.1 mg/mL were not enhanced after 24 h (Fig. S12B). However, at a nearly twofold higher concentration (0.17 mg/mL), AgNPs exerted enhanced antibiofilm effects, with a mean $\log_{10}$ reduction of approximately 1.8 in both the adhered and dispersed fractions; however, these effects were less pronounced than those observed with planktonic bacteria (Fig. S11E). These results were significant in both the adhered and dispersed fractions for both the 96-well induction stirrer ($p = 0.0012$ and $p = 0.0407$, respectively) and

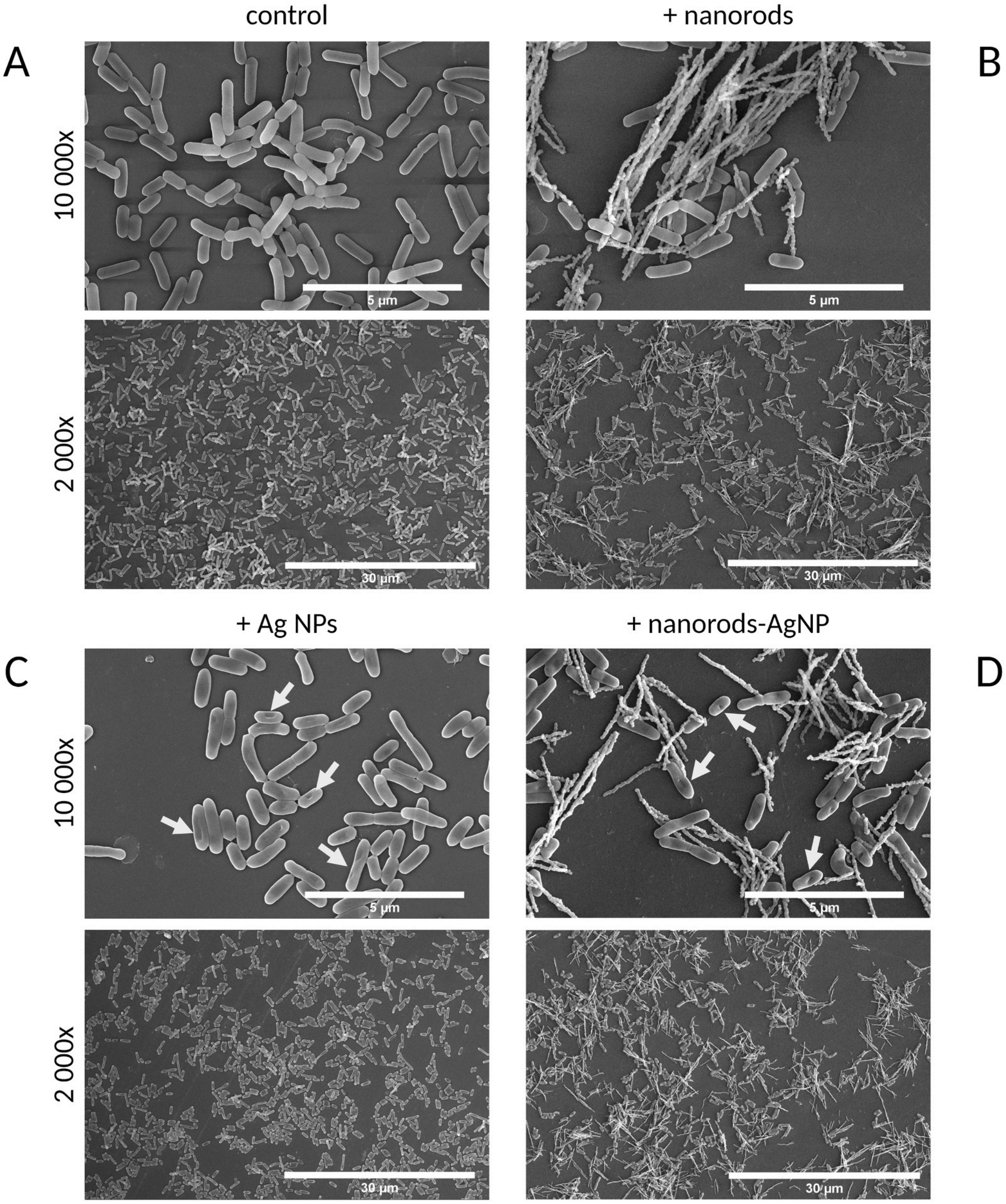

Fig. 7. Representative scanning electron microscopy images of nanoparticle-treated *L. innocua* biofilms. Biofilms were treated with silver nanoparticles (AgNPs) (0.17 mg/mL), nanorods (1 mg/mL), and nanorod-AgNPs (1 mg/mL) for 30 min using a laboratory stirrer at 600 rpm. Untreated biofilm (A), biofilms treated with nanorods (B), AgNPs (C), and nanorod–AgNPs (D). Arrows indicate the observed morphological changes.

laboratory stirrer ($p < 0.0001$ and $p = 0.0006$, respectively). However, the 0.5 $\log_{10}$ reduction effect of nanorod–AgNPs observed after 30 min did not increase but rather diminished after 24 h, showing no difference compared to the untreated control (Fig. 6C, D), which is likely due to effective regrowth. Fluorescence measurements supported these findings, showing significant reductions for both the adhered and dispersed bacterial fractions of AgNP-treated biofilms, for both the 96-well induction stirrer ($p < 0.0001$ and $p = 0.003$, respectively) and laboratory stirrer ($p = 0.008$ and $p = 0.0004$, respectively) (Fig. S6D, E).

This confirms our findings that the effects of AgNPs increase with longer incubation times but are less effective on *L. innocua* biofilms compared to planktonic cells, indicating that *L. innocua* cells in biofilms are more resistant. Additionally, the lack of shaking could affect the movement and efficacy of AgNPs. It was also shown in *L. monocytogenes* biofilms that AgNPs combined with ZnO NPs at higher concentrations exerted antibiofilm effects, which were, however, minimal compared to the control after 24 h, similar to our results [80]. Our CFU and fluorescence measurements revealed that growth of nanorod–AgNP-treated biofilm after 24 h of regrowth was similar to that of the untreated control. We hypothesize that AgNPs exert antibacterial effects through interaction and contact due to Brownian movement. Consequently, immobilization of AgNPs on nanorods decreases the probability of direct contact between AgNPs and bacteria. Therefore, during the 24 h of *L. innocua* regrowth, AgNPs remain in contact with bacterial cells to exert their toxicity, whereas nanorod–AgNPs interact with bacteria only during the 30 min treatment, limiting their effectiveness.

L. innocua biofilms treated with AgNPs, nanorods, and nanorod–AgNPs using a laboratory stirrer were further visualized by SEM (Figs. 7, 8). Bacterial cell length was more heterogeneous in NP-treated than untreated control samples (Fig. S16). Bacterial length significantly differed after 30 min of treatment with AgNPs ($p = 0.0007$) and nanorods ($p < 0.0001$) (Fig. S16A). The median cell lengths in the untreated

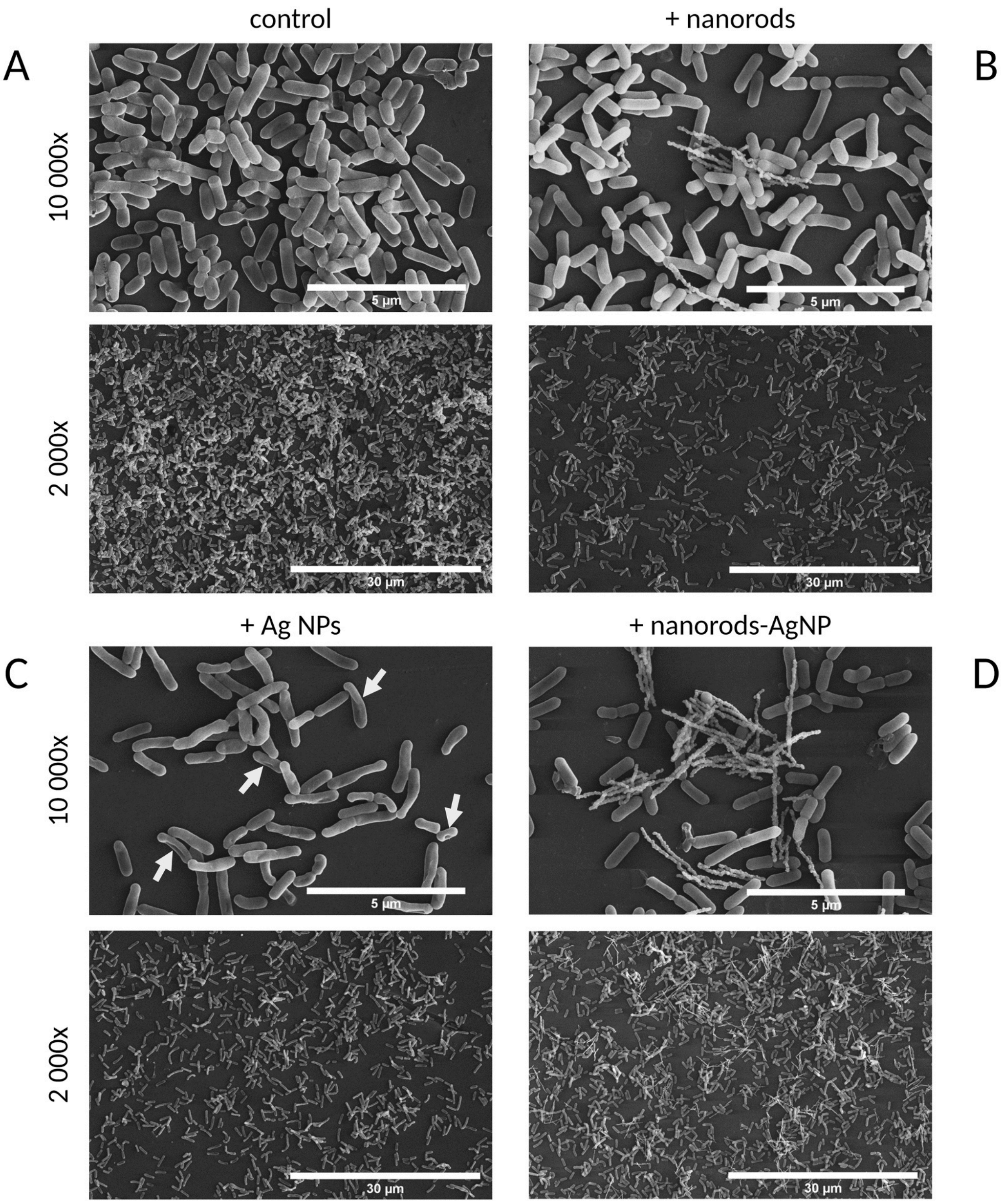

Fig. 8. Representative scanning electron microscopy images of nanoparticle-treated *L. innocua* biofilms after 30 min treatment and a 24 h period of regrowth. Biofilms were treated with silver nanoparticles (AgNPs) (0.17 mg/mL), nanorods (1 mg/mL), and nanorod–AgNPs (1 mg/mL) for 30 min using a laboratory stirrer at 600 rpm, after which they were incubated for 24 h to enable regrowth. Untreated biofilm (A), biofilms treated with nanorods (B), AgNPs (C) and nanorod–AgNPs (D). Arrows indicate the observed morphological changes.

control, AgNP-treated, nanorod-treated, and nanorod–AgNP-treated samples were 1.23 (1.08–1.43), 1.31 (1.08–1.53), 1.31 (1.14–1.47) and 1.26 (1.06–1.48) μm, respectively. Minimal and maximal bacterial lengths were observed in silver-containing samples, ranging from 0.56 μm and up to 2.58 μm for AgNPs and 1.55 μm for nanorod–AgNPs, possibly resulting from a stress response. Conversely, in the untreated control, the minimal and maximal lengths were 0.51 μm and 1.20 μm, respectively. It has previously been reported that *L. monocytogenes* cells can shorten by up to 50% in the presence of AgNPs [81]. Additionally, in AgNP-treated samples, we observed marks on the bacterial surfaces (Fig. 7), which were more frequent and pronounced after 30 min of treatment. The observed morphology was similar to that observed in other studies involving AgNPs [82,83]. Conversely, these morphological changes could also result from sample preparation, during which lyophilization can disrupt the bacterial cell wall.

In SEM images of samples treated with AgNPs, nanorods, and nanorod–AgNPs for 30 min followed by 24 h of regrowth, bacteria appeared less dense in the AgNP-treated sample, indicating a possible stress response (Fig. 8). After 24 h of incubation, AgNP- and nanorod–AgNP-treated bacteria exhibited similar morphological changes, with more frequent and distinct marks on their surfaces compared to those observed after 30 min of treatment. The median lengths of untreated and AgNP-treated bacterial cells were similar: 1.28 (1.07–1.52) μm and 1.27 (1.10–1.47) μm, respectively (Fig. S16B). Conversely, nanorod- and nanorod–AgNP-treated bacterial cells were distinctly shorter than control cells, with median values of 1.22 (1.02–1.50) μm ($p = 0.0491$) and 1.13 (0.88–1.39) μm ($p < 0.0001$), respectively. Maximal bacterial lengths were observed in samples containing silver, i.e., AgNPs and nanorod–AgNPs, reaching 3.42 μm and 3.56 μm, respectively, suggesting growth under stressful conditions with impaired division (Fig. S16B).

SEM revealed that nanorods adhered to the cell surface of *L. innocua* biofilms (Fig. 7). This indicates that rotation of the nanorods in the rotating magnetic field facilitates their contact and adhesion to biofilms, as we have shown is possible for planktonic *L. innocua* as well (Figs. 7, S7). SEM further revealed that clusters of nanorods intertwined with bacterial cells (Fig. 7), suggesting that nanorods affect biofilms without detaching *L. innocua* cells. However, the adhered nanorods prevented the evaluation of bacteria-covered surfaces (compared to the control). Nanorods and nanorod-AgNPs were overgrown with bacteria after 24 h incubation (Fig. 8).

This study evaluated biofilm removal efficacy primarily by measuring cell viability, using CFU and fluorescence assays, and by visualizing sublethal and structural damage in microbial cells, using SEM. A comprehensive understanding of the mechanisms driving these effects is critical for advancing the application of AMPs and AgNPs for the removal of persistent biofilms. Therefore, future studies should employ advanced methods, e.g., flow cytometry, reactive oxygen species quantification, and metabolic activity assays, to elucidate sublethal effects and underlying modes of action. Such investigations will clarify how NP size, morphology, and dynamic actuation contribute to distinct biofilm disruption mechanisms, enabling more targeted and intelligent design.

4. Conclusions

Biofilms are highly persistent and difficult to remove with currently available methods. In this study, we systematically evaluated the effects of AMP characteristics, such as surface roughness and size, on the effectiveness of removing *L. innocua* biofilms. We also employed AgNPs, assessed their toxicity against different microorganisms, and demonstrated a synergistic effect with AMPs, which showed promising results for *L. innocua* biofilm removal. These observations illustrate that biofilm susceptibility to disinfectants, including silver-based treatments, is highly species-dependent, and that intrinsic biological resilience often outweighs the effects of chemical treatments alone. Our findings reinforce the importance of combining mechanical actuation with targeted chemical strategies to achieve synergy for consistent and reproducible biofilm removal across diverse microbial systems.

CRediT authorship contribution statement

Jerica Sabotič: Writing – review & editing, Supervision, Resources, Funding acquisition, Conceptualization. **Laurine Marger:** Writing – review & editing, Writing – original draft, Investigation, Formal analysis. **Parvaneh Esmaeilnejad-Ahranjani:** Methodology, Investigation. **Irena Milosevic:** Writing – review & editing, Supervision, Resources. **Maja Caf:** Writing – review & editing, Writing – original draft, Visualization, Methodology, Investigation, Conceptualization. **Slavko Kralj:** Writing – review & editing, Supervision, Resources, Funding acquisition, Conceptualization. **Vincent Pautu:** Writing – review & editing, Writing – original draft, Investigation. **Fabrice Marger:** Investigation. **Ana Parga:** Investigation. **Nika Janež:** Writing – review & editing, Methodology. **Tanja Zupan:** Investigation. **Aleš Berlec:** Conceptualization. **Nika Zaveršek:** Writing – original draft, Visualization, Methodology, Investigation, Formal analysis, Conceptualization. **Saša Haberl-Meglič:** Writing – review & editing, Investigation. **Mustapha Mekki:** Writing – review & editing, Supervision, Resources.

Funding

This research was funded by the Slovenian Research and Innovation Agency (ARIS) through core funding (P2–0089, P4–0432, and P4–0127) and ARIS projects J3–3079, J7–4420, J4–60079, J3–50123, J2–60047, J2–3043, and L2–60141. This research was also supported by the Swiss National Science Foundation (SNSF) within the Lead agency program (Grant No. 200021E_203577). The authors acknowledge the Center for Electron Microscopy and Microanalysis (Nanocenter, Jožef Stefan Institute, Slovenia) for access to electron microscopy.

Declaration of Competing Interest

The authors declare that they have no known competing financial interests or personal relationships that could have appeared to influence the work reported in this paper.

Acknowledgments

We thank Prof. Dr. Tine Rask Licht, Technical University of Denmark, for the kind gift of plasmid pJEBAN6. We are grateful to Dejan Slokar for help with electroporation and Dr. Aleksandar Sebastijanović for *L. innocua* DsRed clone analysis. Ana Parga gratefully acknowledges support from the Federation of European Microbiological Societies through a Research and Training Grant (No. 1815). We thank dr. Eva Lasic for editing and reviewing a draft of this manuscript.

Appendix A. Supporting information

Supplementary data associated with this article can be found in the online version at doi:10.1016/j.colsurfb.2026.115784

Data availability

Data supporting this study, including CFU counts, fluorescence measurements, *L. innocua* growth curve data, and particle characterization data, are available on Zenodo at https://doi.org/10.5281/zenodo.18246053. Other data for this article, including SEM images of *L. innocua*, are available in the BioImage Archive [84] at https://doi.org/10.6019/S-BIAD2741.

The Supporting Material is available:•

Scheme showing the experimental workflow for biofilm reduction, Fluorescence of used particles. Nanochains (Fig. S1), Scheme showing the experimental workflow for biofilm reduction (Fig. S2), Magnetic stirrers and corresponding magnetic fields (Fig. S3), Effect of treatment in ultrasound bath on planktonic *Listeria innocua* (Fig. S4), Representative SEM image of *Listeria innocua* washed biofilm and CFU counts from *L. innocua* biofilm washing analysis (Fig. S5), Normalized fluorescence intensity of adhered *Listeria innocua* after treatment (Fig. S6), Length distributions and mass magnetization measurements of AMPs (Fig. S7), Log_{10} reduction in CFU values comparing the effects of three AMP sizes (Fig. S8), Log_{10} reduction of planktonic *Listeria innocua* adhesion on AMPs (Fig. S9), Characterization of Ag nanoparticles (AgNPs) and nanorod-AgNPs (Fig. S10), Effects of silver nanoparticles (AgNPs) on the growth of planktonic *Listeria innocua* (Fig. S11), Effects of silver nanoparticles (AgNPs), SiO_2NPs and $AgNO_3$ at various concentrations on the 24 h *Listeria innocua* biofilm, shown as CFU $\log_{10}$ reduction (Fig. S12), Effect of silver nanoparticles (AgNPs) on *E. faecalis* and *C. albicans* 24 h biofilms (Fig. S13), Viability of *Enterococcus faecalis* surface-associated cells after 24 h exposure to silver nanoparticles (AgNPs) during initial adhesion at concentrations of 0.1, 0.01, 0.001, and 0.0001 mg/mL (Fig. S14), Effect of $AgNO_3$ on 24 h *Enterococcus faecalis* biofilms grown on grade 4 titanium plates (Fig. S15), Bacterial cell lengths as measured from SEM images of treated biofilms treated with nanoparticles (Fig. S16) (PDF).•

A video showing nanoparticle rotation in microtiter wells exposed to the conventional laboratory stirrer (MP4).

References

[1] HC Flemming, J. Wingender, U. Szewzyk, P. Steinberg, SA Rice, S. Kjelleberg, Biofilms: an emergent form of bacterial life, Nat. Rev. Microbiol 14 (2016) 563–575, https://doi.org/10.1038/nrmicro.2016.94.

[2] C. Carrascosa, D. Raheem, F. Ramos, A. Saraiva, A. Raposo, Microbial biofilms in the food industry—A comprehensive review, Int J. Environ. Res Public Health 18 (2021) 2014, https://doi.org/10.3390/IJERPH18042014.

[3] RR. Ray, Dental biofilm: Risks, diagnostics and management, Biocatal. Agric. Biotechnol. 43 (2022) 102381, https://doi.org/10.1016/J.BCAB.2022.102381.

[4] HC Flemming, J. Wingender, The biofilm matrix, Nat. Rev. Microbiol 8 (2010) 623–633, https://doi.org/10.1038/nrmicro2415.

[5] HC Flemming, J. Wingender, U. Szewzyk, P. Steinberg, SA Rice, S. Kjelleberg, Biofilms: an emergent form of bacterial life, Nat. Rev. Microbiol. 14 (9) (2016) 563–575, https://doi.org/10.1038/nrmicro.2016.94, 2016;14.

[6] HY Liu, EL Prentice, MA. Webber, Mechanisms of antimicrobial resistance in biofilms, Npj Antimicrob. Resist. 2 (1) (2024) 1–10, https://doi.org/10.1038/s44259-024-00046-3, 2024;2.

[7] H. Ramadan, M. Al-Ashmawy, AM Soliman, M. Elbediwi, I. Sabeq, M. Yousef, et al., Whole-genome sequencing of *Listeria innocua* recovered from retail milk and dairy products in Egypt, Front Microbiol 14 (2023), https://doi.org/10.3389/FMICB.2023.1160244.

[8] N. Janež, M. Ladányi, M. Sterniša, B. Jug, T. Zupan, T. Peternel, et al., Exposure to specific fungal lectins during adhesion impairs biofilm formation of *Listeria* on polystyrene, Micro Biotechnol. 17 (2024), https://doi.org/10.1111/1751-7915.70040.

[9] A. Zawiasa, M. Schmidt, A. Olejnik-Schmidt, Phage-based control of *listeria innocua* in the food industry: a strategy for preventing *listeria monocytogenes* persistence in biofilms, Viruses 17 (2025) 482, https://doi.org/10.3390/V17040482.

[10] S. Galié, C. García-Gutiérrez, EM Miguélez, CJ Villar, F. Lombó, Biofilms in the food industry: health aspects and control methods, Front. Microbiol. 9 (2018) 315815, https://doi.org/10.3389/FMICB.2018.00898/BIBTEX.

[11] I. Kaszoni-Rückerl, A. Mustedanagic, S. Muri-Klinger, K. Brugger, KH Wagner, M. Wagner, et al., Predominance of distinct *Listeria innocua* and *Listeria monocytogenes* in recurrent contamination events at dairy processing facilities, Microorganisms 8 (2020), https://doi.org/10.3390/microorganisms8020234.

[12] J. Sharma, S. Jhamb, M. Mehta, J. Bhushan, SB Bhardwaj, A. Kaur, Prevalence of *Enterococcus faecalis* in refractory endodontic infections: a microbiological study, J. Conserv. Dent. Endod. 28 (2025) 462–467, https://doi.org/10.4103/JCDE.JCDE_871_24.

[13] L. Coronado-Castellote, Jiménez-Soriano Y. Clinical and microbiological diagnosis of oral candidiasis, J. Clin. Exp. Dent. 5 (2013) 279–286, https://doi.org/10.4317/jced.51242.

[14] V. Scholtz, J. Pazlarova, H. Souskova, J. Khun, J. Julak, Nonthermal plasma — A tool for decontamination and disinfection, Biotechnol. Adv. 33 (2015) 1108–1119, https://doi.org/10.1016/j.biotechadv.2015.01.002.

[15] Evelyn, FVM. Silva, High pressure processing of milk: Modeling the inactivation of psychrotrophic *Bacillus cereus* spores at 38–70 °C, J. Food Eng. 165 (2015) 141–148, https://doi.org/10.1016/j.jfoodeng.2015.06.017.

[16] MA Bayoumi, RM Kamal, SF Abd El Aal, EI. Awad, Assessment of a regulatory sanitization process in Egyptian dairy plants in regard to the adherence of some food-borne pathogens and their biofilms, Int J. Food Microbiol 158 (2012) 225–231, https://doi.org/10.1016/J.IJFOODMICRO.2012.07.021.

[17] J. Bang, A. Hong, H. Kim, LR Beuchat, MS Rhee, Y. Kim, et al., Inactivation of *Escherichia coli* O157:H7 in biofilm on food-contact surfaces by sequential treatments of aqueous chlorine dioxide and drying, Int J. Food Microbiol 191 (2014) 129–134, https://doi.org/10.1016/J.IJFOODMICRO.2014.09.014.

[18] P. Stiefel, S. Mauerhofer, J. Schneider, K. Maniura-Weber, U. Rosenberg, Q. Ren, Enzymes enhance biofilm removal efficiency of cleaners, Antimicrob. Agents Chemother. 60 (2016) 3647–3652, https://doi.org/10.1128/AAC.00400-16/SUPPL_FILE/ZAC006165242SO1.PDF.

[19] J. Coronel-León, AM Marqués, J. Bastida, A. Manresa, Optimizing the production of the biosurfactant lichenysin and its application in biofilm control, J. Appl. Microbiol 120 (2016) 99–111, https://doi.org/10.1111/JAM.12992.

[20] L. Iacumin, M. Manzano, G. Comi, L. Iacumin, M. Manzano, G. Comi, Phage inactivation of *Listeria monocytogenes* on San Daniele dry-cured ham and elimination of biofilms from equipment and working environments, Microorganisms 4 (2016), https://doi.org/10.3390/MICROORGANISMS4010004.

[21] H. Koo, RN Allan, RP Howlin, P. Stoodley, L. Hall-Stoodley, Targeting microbial biofilms: Current and prospective therapeutic strategies, Nat. Rev. Microbiol 15 (2017), https://doi.org/10.1038/nrmicro.2017.99.

[22] A.B. Seabra, M.T. Pelegrino, P.S. Haddad, Antimicrobial applications of superparamagnetic Iron oxide nanoparticles: Perspectives and challenges. Nanostructures for Antimicrobial Therapy: Nanostructures in Therapeutic Medicine Series, 2017, pp. 531–550, https://doi.org/10.1016/B978-0-323-46152-8.00024-X.

[23] D. Banerjee, P.M. Shivapriya, P.K. Gautam, K. Misra, A.K. Sahoo, S.K. Samanta, A review on basic biology of bacterial biofilm infections and their treatments by Nanotechnology-Based Approaches, Proc. Natl. Acad. Sci. India Sect. B - Biol. Sci. 90 (2020) 243–259, https://doi.org/10.1007/s40011-018-01065-7.

[24] R.M. Pinto, F.A. Soares, S. Reis, C. Nunes, P. Van Dijck, Innovative strategies toward the disassembly of the EPS matrix in bacterial biofilms, Front Microbiol 11 (2020), https://doi.org/10.3389/fmicb.2020.00952.

[25] S. Kralj, C. Da Silva, S. Nemec, M. Caf, I. Fourquaux, MP Rols, et al., Dynamically assembling magnetic nanochains as new generation of swarm-type magneto-mechanical nanorobots affecting biofilm integrity, Adv. Health Mater. (2025), https://doi.org/10.1002/adhm.202403736.

[26] S. Majidi, FZ Sehrig, SM Farkhani, MS Goloujeh, A. Akbarzadeh, Current methods for synthesis of magnetic nanoparticles, Artif. Cells Nanomed. Biotechnol. 44 (2014), https://doi.org/10.3109/21691401.2014.982802.

[27] SM Dadfar, D. Camozzi, M. Darguzyte, K. Roemhild, P. Varvarà, J. Metselaar, et al., Size-isolation of superparamagnetic iron oxide nanoparticles improves MRI, MPI and hyperthermia performance, J. Nanobiotechnol. 18 (2020), https://doi.org/10.1186/s12951-020-0580-1.

[28] M. Caf, P. Esmaeilnejad-Ahranjani, J. Kolosnjaj-Tabi, J. Sabotič, A. Berlec, N. Zaveršek, et al., Magnetic field-driven strategies for biofilm disruption: from iron oxide nanoparticles to adaptive swarms of magnetic microrobots, ACS Nano 20 (2026), https://doi.org/10.1021/ACSNANO.5C14390.

[29] HF Hetta, YN Ramadan, AI Al-Harbi, E. A. Ahmed, B. Battah, NH Abd Ellah, et al., Nanotechnology as a promising approach to combat multidrug resistant bacteria: A comprehensive review and future perspectives, Biomedicines 11 (2023), https://doi.org/10.3390/biomedicines11020413.

[30] L. Wang, C. Hu, L. Shao, The antimicrobial activity of nanoparticles: present situation and prospects for the future, Int J. Nanomed. 12 (2017) 1227–1249, https://doi.org/10.2147/IJN.S121956.

[31] R. Dinali, A. Ebrahiminezhad, M. Manley-Harris, Y. Ghasemi, A. Berenjian, Iron oxide nanoparticles in modern microbiology and biotechnology, Crit. Rev. Microbiol 43 (2017) 493–507, https://doi.org/10.1080/1040841X.2016.1267708.

[32] K. Quan, G. Jiang, J. Liu, Z. Zhang, Y. Ren, HJ Busscher, et al., Influence of interaction between surface-modified magnetic nanoparticles with infectious biofilm components in artificial channel digging and biofilm eradication by antibiotics *in vitro* and *in vivo*, Nanoscale 13 (2021) 4644–4653, https://doi.org/10.1039/d0nr08537e.

[33] M. Šavli, M. Černila, M. Caf, A. Zahirović, N. Zaveršek, et al., Magnetomechanical detachment of bacterial biofilms using anisotropic magnetic iron oxide nanochains, ACS Appl. Bio Mater. 8 (2025), https://doi.org/10.1021/ACSABM.5C01029.

[34] PR More, S. Pandit, A.De Filippis, G. Franci, I. Mijakovic, M. Galdiero, Silver Nanoparticles: Bactericidal and mechanistic approach against drug resistant pathogens, Microorganisms 11 (2023) 369, https://doi.org/10.3390/MICROORGANISMS11020369. Page 369 2023;11.

[35] M. Solomon, AM Holban, B. Bălăceanu-Gurău, LM Dițu, A. Alberts, AM Grumezescu, et al., Silver nanoparticles functionalized with polymeric substances to reduce the growth of planktonic and biofilm opportunistic pathogens, Int J. Mol. Sci. 26 (2025), https://doi.org/10.3390/IJMS26093930.

[36] MF Akhter, M. Irshad, S. Ali, M. Summer, Noor-ul-ain-Zulfiqar, MF Akhter, et al., Understanding the silver nanotoxicity: mechanisms, risks, and mitigation strategies, J. Nanopart. Res. 27 (2025) 1–18, https://doi.org/10.1007/S11051-025-06273-7/FIGURES/3.

[37] AS Joshi, P. Singh, I. Mijakovic, Interactions of gold and silver nanoparticles with bacterial biofilms: Molecular interactions behind inhibition and resistance, Int. J. Mol. Sci. 21 (2020) 7658, https://doi.org/10.3390/IJMS21207658. Page 7658 2020;21.

[38] T. Polajžer, M. Kranjc, S. Kralj, M. Caf, R. Romih, S. Hudoklin, et al., Limited efficacy of nanoparticle-assisted electroporation for membrane permeabilization and gene electrotransfer, Pharmaceutics 17 (2025), https://doi.org/10.3390/PHARMACEUTICS17080964/S1.

[39] S. Kralj, F. Longobardo, D. Iglesias, M. Bevilacqua, C. Tavagnacco, A. Criado, et al., Ex-Solution synthesis of Sub-5-nm FeOx nanoparticles on mesoporous hollow N,O-Doped carbon nanoshells for electrocatalytic oxygen reduction, ACS Appl. Nano Mater. 2 (2019), https://doi.org/10.1021/acsanm.9b01511.

[40] M. Tadic, S. Kralj, M. Jagodic, D. Hanzel, D. Makovec, Magnetic properties of novel superparamagnetic iron oxide nanoclusters and their peculiarity under annealing treatment, Appl. Surf. Sci. 322 (2014) 255–264, https://doi.org/10.1016/j.apsusc.2014.09.181.

[41] S. Nemec, S. Kralj, A versatile interfacial coassembly method for fabrication of tunable silica shells with radially aligned dual mesopores on diverse magnetic core nanoparticles, ACS Appl. Mater. Interfaces 13 (2021) 1883–1894, https://doi.org/10.1021/acsami.0c17863.

[42] S. Kralj, D. Makovec, Magnetic assembly of superparamagnetic iron oxide nanoparticle clusters into nanochains and nanobundles, ACS Nano 9 (2015) 9700–9707, https://doi.org/10.1021/ACSNANO.5B02328.

[43] R. Peter, S. Kralj, I. Pološčić, M. Perčić, M. Kocijan, D. Jardas Babić, et al., Ultra-thin ZnO coatings on microstructured γ-Fe2O3 thin films prepared by atomic layer deposition for enhanced photocatalysis, Mater. Chem. Phys. 346 (2025) 131373, https://doi.org/10.1016/J.MATCHEMPHYS.2025.131373.

[44] S. Kralj, D. Makovec, S. Čampelj, M. Drofenik, Producing ultra-thin silica coatings on iron-oxide nanoparticles to improve their surface reactivity, J. Magn. Magn. Mater. 322 (2010) 1847–1853, https://doi.org/10.1016/j.jmmm.2009.12.038.

[45] S. Kralj, M. Drofenik, D. Makovec, Controlled surface functionalization of silica-coated magnetic nanoparticles with terminal amino and carboxyl groups, J. Nanopart. Res. 13 (2011) 2829–2841, https://doi.org/10.1007/s11051-010-0171-4.

[46] S. Kralj, D. Makovec, The chemically directed assembly of nanoparticle clusters from superparamagnetic iron-oxide nanoparticles, RSC Adv. 4 (2014) 13167–13171, https://doi.org/10.1039/c4ra00776j.

[47] S. Gyergyek, D. Makovec, M. Drofenik, Colloidal stability of oleic- and ricinoleic-acid-coated magnetic nanoparticles in organic solvents, J. Colloid Interface Sci. 354 (2011) 498–505, https://doi.org/10.1016/j.jcis.2010.11.043.

[48] B. Bellich, N. Janež, M. Sterniša, A. Klančnik, N. Ravenscroft, R. Rizzo, et al., Characterisation of a new cell wall teichoic acid produced by *Listeria innocua* ŽM39 and analysis of its biosynthesis genes, Carbohydr. Res 511 (2022) 108499, https://doi.org/10.1016/J.CARRES.2021.108499.

[49] L. Ma, G. Zhang, MP. Doyle, Green fluorescent protein labeling of *Listeria, Salmonella*, and *Escherichia coli* O157:H7 for safety-related studies, PLoS One 6 (2011) e18083, https://doi.org/10.1371/JOURNAL.PONE.0018083.

[50] JB Andersen, BB Roldgaard, AB Lindner, BB Christensen, TR. Licht, Construction of a multiple fluorescence labelling system for use in co-invasion studies of *Listeria monocytogenes*, BMC Microbiol 6 (2006) 86, https://doi.org/10.1186/1471-2180-6-86.

[51] NT Wirth, J. Funk, S. Donati, PI. Nikel, QurvE: user-friendly software for the analysis of biological growth and fluorescence data, Nat. Protoc. 18 (2023) 2401–2403, https://doi.org/10.1038/S41596-023-00850-7.

[52] M. Kahm, G. Hasenbrink, H. Lichtenberg-Fraté, J. Ludwig, M. Kschischo, grofit: Fitting biological growth curves with, R. J. Stat. Softw. 33 (2010) 1–21, https://doi.org/10.18637/JSS.V033.I07.

[53] Q. Geissmann, OpenCFU, a new free and open-source software to count cell colonies and other circular objects, PLoS One 8 (2013) e54072, https://doi.org/10.1371/JOURNAL.PONE.0054072.

[54] Y. Chen, C. Qian, N. Miao, Atomic force microscopy indentation to determine mechanical property for polystyrene–silica core–shell hybrid particles with controlled shell thickness, Thin Solid Films 579 (2015) 57–63, https://doi.org/10.1016/J.TSF.2015.02.049.

[55] W. Zhang, J. Li, Y. Xing, X. Nie, F. Lang, S. Yang, et al., Experimental study on the thickness-dependent hardness of SiO2 thin films using nanoindentation, Coatings 11 (2020) 23, https://doi.org/10.3390/COATINGS11010023.

[56] B. Kundukad, T. Seviour, Y. Liang, SA Rice, S. Kjelleberg, PS. Doyle, Mechanical properties of the superficial biofilm layer determine the architecture of biofilms, Soft Matter 12 (26) (2016) 5718, https://doi.org/10.1039/C6SM00687F.

[57] S. Silva, P. Teixeira, R. Oliveira, J. Azeredo, Adhesion to and viability of *Listeria monocytogenes* on food contact surfaces, J. Food Prot. 71 (2008) 1379–1385, https://doi.org/10.4315/0362-028X-71.7.1379.

[58] ET Sumrall, AP Keller, Y. Shen, MJ. Loessner, Structure and function of *Listeria* teichoic acids and their implications, Mol. Microbiol 113 (2020) 627–637, https://doi.org/10.1111/MMI.14472.

[59] N. Janež, B. Škrlj, M. Sterniša, A. Klančnik, J. Sabotič, The role of the *Listeria monocytogenes* surfactome in biofilm formation, Micro Biotechnol. 14 (2021) 1269–1281, https://doi.org/10.1111/1751-7915.13847.

[60] FP Gordesli-Duatepe, BJ Park, LH Kawas, NI. Abu-Lail, Atomic force microscopy investigation of the contributions of *Listeria monocytogenes* cell-wall biomacromolecules to their adherence and mechanics, J. Phys. Chem. B 124 (2020) 5872–5883, https://doi.org/10.1021/ACS.JPCB.0C04025/SUPPL_FILE/JP0C04025_SI_001.PDF.

[61] HQ Tran, H. Alam, A. Goff, T. Daeneke, M. Bhave, A. Yu, Multifunctional Fe3O4 nanoparticles filled polydopamine hollow rods for antibacterial biofilm treatment, Molecules 28 (2023) 2325, https://doi.org/10.3390/MOLECULES28052325.

[62] T. Bhuyan, AT Simon, S. Maity, AK Singh, SS Ghosh, D. Bandyopadhyay, Magnetotactic T-Budbots to Kill-n-Clean Biofilms, ACS Appl. Mater. Interfaces 12 (2020) 43352–43364, https://doi.org/10.1021/ACSAMI.0C08444/ASSET/IMAGES/LARGE/AM0C08444_0010.JPEG.

[63] CC Mayorga-Martinez, J. Zelenka, K. Klima, M. Kubanova, T. Ruml, M. Pumera, et al., Multimodal-driven magnetic microrobots with enhanced bactericidal activity for biofilm eradication and removal from titanium mesh, Adv. Mater. 35 (2023) 2300191, https://doi.org/10.1002/ADMA.202300191.

[64] V. Pautu, L. Marger, M. Caf, F. Marger, M. Mekki, S. Kralj, et al., Influence of particle size, shape, and magnetic properties on torque-driven biofilm removal using anisotropic magnetic particles, Nanoscale (2026), https://doi.org/10.1039/D6NR00046K.

[65] J. Guo, W. Wei, Y. Zhao, H. Dai, Iron oxide nanoparticles with photothermal performance and enhanced nanozyme activity for bacteria-infected wound therapy, Regen. Biomater. 9 (2022), https://doi.org/10.1093/RB/RBAC041.

[66] KN Shoudho, S. Uddin, MMH Rumon, MS. Shakil, Influence of physicochemical properties of iron oxide nanoparticles on their antibacterial activity, ACS Omega 9 (2024) 33303–33334, https://doi.org/10.1021/ACSOMEGA.4C02822/ASSET/IMAGES/LARGE/AO4C02822_0003.JPEG.

[67] K. Sahoo, S. Kumar, Green synthesis of sub 10 nm silver nanoparticles in gram scale using free impinging jet reactor, Chem. Eng. Process. - Process. Intensif. 165 (2021) 108439, https://doi.org/10.1016/J.CEP.2021.108439.

[68] N. Chauhan, AK Tyagi, P. Kumar, A. Malik, Antibacterial potential of *Jatropha curcas* synthesized silver nanoparticles against food borne pathogens, Front Microbiol 7 (2016) 188541, https://doi.org/10.3389/FMICB.2016.01748/BIBTEX.

[69] J. Du, Z. Yu, J. Jin, J. Liu, Z. Ma, J. Zhao, Silver nanoparticles resistance in *Listeria monocytogenes*: morphologic, virulence and cellular response, Int J. Food Microbiol 442 (2025) 111365, https://doi.org/10.1016/j.ijfoodmicro.2025.111365.

[70] A. Parga, D. Manoil, M. Brundin, A. Otero, GN. Belibasakis, Gram-negative quorum sensing signalling enhances biofilm formation and virulence traits in gram-positive pathogen *Enterococcus faecalis*, J. Oral. Microbiol 15 (2023), https://doi.org/10.1080/20002297.2023.2208901.

[71] TB Schille, JL Sprague, JR Naglik, S. Brunke, B. Hube, Commensalism and pathogenesis of *Candida albicans* at the mucosal interface, Nat. Rev. Microbiol 23 (2025) 525–540, https://doi.org/10.1038/s41579-025-01174-x.

[72] A. Giammarino, L. Verdolini, G. Simonetti, L. Angiolella, A. Giammarino, L. Verdolini, et al., Fungal Biofilm: An overview of the latest nano-strategies, Antibiotics 14 (2025), https://doi.org/10.3390/ANTIBIOTICS14070718.

[73] A. Parga, J. Mattu, GN Belibasakis, KA Kline, JG Leprince, D. Manoil, A polymicrobial perspective into the ecological role of *Enterococcus faecalis* in dental root canal infections, NPJ Biofilms Micro 11 (2025), https://doi.org/10.1038/S41522-025-00722-W.

[74] PR More, S. Pandit, A.De Filippis, G. Franci, I. Mijakovic, M. Galdiero, Silver nanoparticles: Bactericidal and mechanistic approach against drug resistant pathogens, Microorganisms 11 (2023) 369, https://doi.org/10.3390/MICROORGANISMS11020369.

[75] ZM Xiu, QB Zhang, HL Puppala, VL Colvin, PJJ. Alvarez, Negligible particle-specific antibacterial activity of silver nanoparticles, Nano Lett. 12 (2012) 4271–4275, https://doi.org/10.1021/nl301934w.

[76] C. Liu, W. Leng, PJ. Vikesland, Controlled evaluation of the impacts of surface coatings on silver nanoparticle dissolution rates, Environ. Sci. Technol. 52 (2018) 2726–2734, https://doi.org/10.1021/acs.est.7b05622.

[77] C. Liao, Y. Li, SC. Tjong, Bactericidal and cytotoxic properties of silver nanoparticles, Int J. Mol. Sci. 20 (2019) 449, https://doi.org/10.3390/IJMS20020449.

[78] OJ Oziri, Y. Wang, T. Watanabe, S. Uno, M. Maeki, M. Tokeshi, et al., PEGylation of silver nanoparticles by physisorption of cyclic poly(ethylene glycol) for enhanced dispersion stability, antimicrobial activity, and cytotoxicity, Nanoscale Adv. 4 (2022) 532–545, https://doi.org/10.1039/D1NA00720C.

[79] M. Seo, T. Oh, S. Bae, Antibiofilm activity of silver nanoparticles against biofilm forming *Staphylococcus pseudintermedius* isolated from dogs with otitis externa, Vet. Med Sci. 7 (2021) 1551–1557, https://doi.org/10.1002/VMS3.554.

[80] LE Tadielo, EA Rodrigues dos Santos, PR Lopes Melo, LC Bastos Juliano, EC da Silva, BL da Silva, et al., Inhibition of multispecies biofilm formation by *Listeria monocytogenes, Salmonella* spp., and associated microbiota using thymol, carvacrol, lactic and acetic acid, and silver and zinc oxide nanoparticles, LWT (2025) 118412, https://doi.org/10.1016/J.LWT.2025.118412.

[81] K. Markowska, AM Grudniak, B. Milczarek, KI. Wolska, The effect of silver nanoparticles on *Listeria monocytogenes* PCM2191 Peptidoglycan metabolism and cell permeability, Pol. J. Microbiol 67 (2018) 315, https://doi.org/10.21307/PJM-2018-037.

[82] B. Ahmed, F. Ameen, A. Rizvi, K. Ali, H. Sonbol, A. Zaidi, et al., Destruction of cell topography, morphology, membrane, inhibition of respiration, biofilm formation, and bioactive molecule production by nanoparticles of Ag, ZnO, CuO, TiO2, and Al2O3 toward beneficial soil bacteria, ACS Omega 5 (2020) 7861–7876, https://doi.org/10.1021/ACSOMEGA.9B04084.

[83] Y. Yan, G. Li, M. Su, H. Liang, *Scutellaria baicalensis* polysaccharide-mediated green synthesis of smaller silver nanoparticles with enhanced antimicrobial and antibiofilm activity, ACS Appl. Mater. Interfaces 16 (2024) 45289–45306, https://doi.org/10.1021/acsami.4c07770.

[84] J. McEntyre, U. Sarkans, A. Brazma, The biostudies database, Mol. Syst. Biol. 11 (2015), https://doi.org/10.15252/MSB.20156658, 847–847.